

Article

# Fluorescent Single-Core and Multi-Core Nanoprobes as Cell Trackers and Magnetic Nanoheaters

Pelayo García Acevedo <sup>\*,†</sup>, Manuel A. González Gómez <sup>\*,†</sup>, Ángela Arnosa Prieto ,  
Lisandra De Castro Alves , Román Seco Gudiña , Yolanda Piñeiro  and José Rivas 

NANOMAG Laboratory, Applied Physics Department and iMATUS Materials Institute, Universidade de Santiago de Compostela, 15782 Santiago de Compostela, Spain; angela.arnosa@usc.es (Á.A.P.); lisandracristina.decastro@usc.es (L.D.C.A.); roman.seco@rai.usc.es (R.S.G.); y.pineiro.redondo@usc.es (Y.P.); jose.rivas@usc.es (J.R.)

\* Correspondence: pelayo.garcia.acevedo@usc.es (P.G.A.); manuelantonio.gonzalez@usc.es (M.A.G.G.);

Tel.: +34-881813097 (P.G.A. & M.A.G.G.)

† The authors contributed equally to this work.

**Abstract:** Iron oxide magnetic nanoparticles (MNPs) have been widely studied due to their versatility for diagnosis, tracking (magnetic resonance imaging (MRI)) and therapeutic (magnetic hyperthermia and drug delivery) applications. In this work, iron oxide MNPs with different single-core (8–40 nm) and multi-core (140–200 nm) structures were synthesized and functionalized by organic and inorganic coating materials, highlighting their ability as magnetic nanotools to boost cell biotechnological procedures. Single core Fe<sub>3</sub>O<sub>4</sub>@PDA, Fe<sub>3</sub>O<sub>4</sub>@SiO<sub>2</sub>-FITC-SiO<sub>2</sub> and Fe<sub>3</sub>O<sub>4</sub>@SiO<sub>2</sub>-RITC-SiO<sub>2</sub> MNPs were functionalized with fluorescent components with emission at different wavelengths, 424 nm (polydopamine), 515 (fluorescein) and 583 nm (rhodamine), and their ability as transfection and imaging agents was explored with HeLa cells. Moreover, different multi-core iron oxide MNPs (Fe<sub>3</sub>O<sub>4</sub>@CS, Fe<sub>3</sub>O<sub>4</sub>@SiO<sub>2</sub> and Fe<sub>3</sub>O<sub>4</sub>@Citrate) coated with organic (citrate and chitosan, CS) and inorganic (silica, SiO<sub>2</sub>) shells were tested as efficient nanoheaters for magnetic hyperthermia applications for mild thermal heating procedures as an alternative to simple structures based on single-core MNPs. This work highlights the multiple abilities offered by the synergy of the use of external magnetic fields applied on MNPs and their application in different biomedical approaches.

**Keywords:** iron oxide magnetic nanoparticles; nanomagnetism; cell tracking; magnetic hyperthermia; nanowarming



**Citation:** García Acevedo, P.; González Gómez, M.A.; Arnosa Prieto, Á.; De Castro Alves, L.; Seco Gudiña, R.; Piñeiro, Y.; Rivas, J. Fluorescent Single-Core and Multi-Core Nanoprobes as Cell Trackers and Magnetic Nanoheaters. *Magnetochemistry* **2022**, *8*, 83. <https://doi.org/10.3390/magnetochemistry8080083>

Academic Editor: Alexey Chubarov

Received: 30 June 2022

Accepted: 26 July 2022

Published: 29 July 2022

**Publisher's Note:** MDPI stays neutral with regard to jurisdictional claims in published maps and institutional affiliations.



**Copyright:** © 2022 by the authors. Licensee MDPI, Basel, Switzerland. This article is an open access article distributed under the terms and conditions of the Creative Commons Attribution (CC BY) license (<https://creativecommons.org/licenses/by/4.0/>).

## 1. Introduction

The numerous advances produced in recent decades in the field of magnetic nanoparticles synthesis have provided several mature routes, such as coprecipitation, a simple and cost-effective procedure but with a production of lower crystallinity and higher polydispersity MNPs [1]; hydrothermal processes, based on the use of a water solvent but whose high temperature and pressure produce higher energetic costs [2]; the solvothermal method that allows morphological control from simple structures based on single-core MNPs [3] to complex structures formed by multiple cores [4]; or thermal decomposition, which allows the obtaining of monodisperse MNPs with high crystallinity and improved magnetic properties but whose disadvantages are higher production costs, long-time reactions and particles with hydrophobic surfaces [5]. This plethora of synthetic routes has allowed the design of MNPs with various morphologies, such as cubic, spherical or hexagonal shapes [6], and sizes, from ultra-small (<5 nm) [7] to large MNPs [8], with different architectures from single magnetic core to multi-core structures [9], with a direct control on their physicochemical properties, for on-demand applications. Moreover, the possibility of functionalizing MNPs with different coating materials, organic (polymers, such as polyethyleneimine (PEI), polydopamine (PDA), polyacrylic acid (PAA), etc.) and

inorganic ( $\text{SiO}_2$ , carbon or graphene) or with biological moieties (proteins, polypeptides, antibodies, etc.), allows the production of multi-functional nanostructures for an extended list of applications that goes beyond the use of their magnetic functionality of MNPs [10].

The most remarkable property of sufficiently small MNPs is superparamagnetism (SPM) [11], in which the multidomain structure of bulk ferromagnetic materials becomes a single magnetic domain, whose magnetic moment fluctuates with thermal energy, above the so known blocking temperature,  $T_B$ , presenting negligible coercivity and remanence values. If no magnetic field,  $H$ , is applied at temperatures above the  $T_B$ , SPM ensures the absence of magnetic interactions, avoiding the occurrence of embolism problems which is of outmost importance in *in vivo* uses. Moreover, the full magnetic control achieved by the MNPs switching on and off by applying an external  $H$  expands the applications of MNPs for different biomedical procedures and places them in a leading position in nanomedicine research [12].

Therefore, MNPs can be found as contrast agents in medical imaging processes either by magnetic resonance imaging (MRI), magnetic particle imaging (MPI) [13] or magnetic particle spectroscopy (MPS) [14,15]. Conventionally used gadolinium-based compounds as contrast agents in MRI, present toxicity and side effects [16] and opens the way for the development of iron oxides MNPs with improved performance as contrast agents [17,18] that can be supplemented, through the addition of fluorescent components such as poly-dopamine, fluorescein, or rhodamine, with optical properties for combined MRI and optical imaging. One of the main strategies to develop hybrid fluorescent MNPs is the design core-shell structures based on inorganic  $\text{SiO}_2$  coatings as supporting material to anchor different fluorophores [19,20]. The incorporation of quantum dots (QDs) in the  $\text{SiO}_2$  shell provides fluorescent nanomaterials with excellent optical properties [21], especially those based on carbon dots due to low toxicity [22,23]. Additionally, polymers can be grafted on the MNPs surface, being especially important in the use of MNPs conjugated with PDA, which is a current area of interest [24], allowing for the frugal designs of fluorescent nanoparticles [25,26] or nanorods [27] or even more complex structures, such as fluorescent mesoporous silica [28].

This hybrid strategy compensates the limitations of both imaging techniques, such as the low sensitivity of MRI or the low spatial resolution and low penetration depth of optical imaging techniques, with a penetration depth of MRI and the high sensitivity and cost-effectiveness of optical imaging techniques [29]. The benefits of combined imaging strategies for *in vivo* disease diagnosis, as well as the *in situ* monitoring of living cells [30], has boosted the design of multifunctional nanomaterials capable of acting as dual imaging agents [31].

In addition, MNPs can be used as heat sources at the nanoscale taking advantage of Néel and Brown relaxation processes, in magnetic hyperthermia processes for oncological therapies [32], that have led to a clinically applied solution for glioblastoma treatment (MAGFORCE). In the last times, magnetic hyperthermia has also emerged as a novel technique known as nanowarming, where the homogeneous heating produced by MNPs injected in organs submitted to cryopreservation makes it possible to rewarm large volumes of tissues preventing serious damages due to slow and nonuniform heating [33,34]. Especially interesting is the clustering of several MNPs as a potential way to improve the heating efficiency in hyperthermia processes compared to individually organized MNPs [35]. Different strategies have been reported to produce complex structures, such as nanoparticles clusters in a CTAB-mediated oil-in-water emulsion system [36], super-nanoparticles [37], or silica coated magnetic nanocapsules [38]. In this regard, solvothermal methods [39], characterized by a one-step synthesis, allows the design of multi-core MNPs with tailored physicochemical properties by varying the reactive agents used. This has recently allowed the variation of the MNPs size from 125 to 539 nm by varying the surfactant concentration, allowing the improvement of the heating efficiency in magnetic hyperthermia processes. However, despite obtaining specific absorption rate (SAR) values close to  $100 \text{ Wg}^{-1}$  for the largest MNPs (359 and 539 nm), under the ap-

plication of a magnetic field of  $24 \text{ kAm}^{-1}$ , the SAR values decay when the nanoparticle size decreases up to 125 nm ( $\text{SAR} = 20.8 \text{ Wg}^{-1}$ ) and 180 nm ( $49.7 \text{ Wg}^{-1}$ ) [40]. Since the reported optimal nanoparticle size for cellular uptake is 50 nm and after observing a decrease in efficiency for larger MNPs (70–240 nm) [41], a reduction in the size of multi-core MNPs as nanoheaters without worsening their heating efficiency would be an advantage. Smaller iron oxide MNPs clusters with diameters of around 70–130 nm, 100 nm, or 158 nm were obtained presenting reduced SAR values of  $10\text{--}35 \text{ Wg}^{-1}$  [42],  $22.8 \text{ Wg}^{-1}$  [43] and  $60 \text{ Wg}^{-1}$  [44], respectively, highlighting the correlation of heating efficiency and size. Composition can be also customized to increase SAR, as several studies demonstrate the analysis of the effect of Mn or Co in different ferrites:  $\text{MnFe}_2\text{O}_4$  ( $D = 54 \text{ nm}$ ,  $\text{SAR} = 390 \text{ Wg}^{-1}$ ) [45],  $\text{MnFe}_2\text{O}_4$  ( $D = 75 \text{ nm}$ ,  $\text{SAR} = 104 \text{ Wg}^{-1}$ ),  $\text{CoMn}_2\text{O}_4$  ( $D = 95 \text{ nm}$ ,  $\text{SAR} = 223 \text{ Wg}^{-1}$ ) [46] or  $\text{MnFe}_2\text{O}_4$  ( $D = 106 \text{ nm}$ ,  $\text{SAR} 332 \text{ Wg}^{-1}$ ) [47]. However, these last materials increase their SAR values at the expenses of higher toxicity compared to maghemite/magnetite-based MNPs, questioning their clinical applicability [48].

Therefore, versatility, cost-effectiveness, good magnetic response and biocompatibility of iron oxide MNPs, compared to other magnetic materials, explain their leading role in combination with other materials, such as biopolymers, hydrogels, inorganic nanostructures (mesoporous silica, aluminum hydroxide, etc.), for producing advanced formulations of scaffolds for tissue engineering, theragnostic agents or detection platforms [49].

In this work, the ability of iron oxide MNPs as magnetic nanotools to boost cell biotechnological procedures was shown by studying their applicability as cell trackers and nanoheaters for magnetic hyperthermia and nanowarming processes. By means of thermal decomposition, co-precipitation and solvothermal methods, magnetic cores with different physicochemical properties were obtained and coated with inorganic shells using Stöber and microemulsion methods to produce two batches of MNPs with single core and multi-core structure. Single core MNPs were functionalized using different techniques with fluorescent entities, such as polydopamine ( $\lambda_{\text{em}} = 424 \text{ nm}$ ), fluorescein ( $\lambda_{\text{em}} = 515 \text{ nm}$ ) and rhodamine ( $\lambda_{\text{em}} = 583 \text{ nm}$ ), providing fluorescent MNPs,  $\text{Fe}_3\text{O}_4@\text{PDA}$ ,  $\text{Fe}_3\text{O}_4@\text{SiO}_2\text{-RITC-SiO}_2$  and  $\text{Fe}_3\text{O}_4@\text{SiO}_2\text{-FITC-SiO}_2$  MNPs in order to test their ability as magnetic tracers in a cellular isolation process assisted by external magnetic fields in HeLa cells was subsequently demonstrated. On the other hand, different strategies for the design of MNPs with multi-core structure were studied with the aim of comparing the clustering effects in magnetic hyperthermia processes, which is of current interest due to the improved efficiency versus simpler structures based on single MNPs. In this way, the heating capacity of multi-core MNPs ( $\text{Fe}_3\text{O}_4@\text{CS}$ ,  $\text{Fe}_3\text{O}_4@\text{Citrate}$  and  $\text{Fe}_3\text{O}_4@\text{SiO}_2$ ) of sizes between 140–200 nm was studied by applying external magnetic fields for their use in magnetic hyperthermia and nanowarming processes. In this case, SAR values up to  $100 \text{ Wg}^{-1}$  were obtained for  $\text{Fe}_3\text{O}_4@\text{Citrate}$  MNPs, significantly improving the values obtained using  $\text{Fe}_3\text{O}_4@\text{CS}$ , despite their smaller size. On the other hand, the encapsulation of  $\text{Fe}_3\text{O}_4@\text{PEG}$  MNPs in  $\text{SiO}_2$  coatings allowed the obtaining of SAR values similar to those of  $\text{Fe}_3\text{O}_4@\text{Citrate}$ , being of special interest due to the lower energy cost of this type of synthesis compared to the solvothermal method.

## 2. Materials and Methods

### 2.1. Chemicals

All chemicals used in the synthetic processes were used as received without further purification. Iron(III) chloride hexahydrate ( $\text{FeCl}_3 \cdot 6\text{H}_2\text{O}$ , 99%), iron(II) sulphate heptahydrate ( $\text{FeSO}_4 \cdot 7\text{H}_2\text{O}$ , 99%), iron-oleate complex, polyethylenglycol (PEG,  $\text{C}_{2n}\text{H}_{4n+2}\text{O}_{n+1}$ , Mw: 300), sodium citrate dihydrate ( $\text{C}_6\text{H}_9\text{Na}_3\text{O}_9 \cdot 2\text{H}_2\text{O}$ , 98%), tetraethyl orthosilicate (TEOS,  $\text{SiC}_8\text{H}_{20}\text{O}_4$ , 98%), chitosan (CS,  $\text{C}_{56}\text{H}_{103}\text{N}_9\text{O}_{39}$ , deacetylated chitin, low molecular weight), dopamine hydrochloride ( $\text{C}_8\text{H}_{11}\text{NO}_2 \cdot \text{HCl}$ , 98%), polyvinylpyrrolidone (PVP,  $\text{C}_6\text{H}_9\text{NO}$ , Mw: 55,000), fluorescein isothiocyanate (FITC,  $\text{C}_{21}\text{H}_{11}\text{NO}_5\text{S}$ , 90%), rhodamine B isothiocyanate (RITC,  $\text{C}_{28}\text{H}_{30}\text{N}_2\text{SO}$  mixture of isomers), 3-Aminopropyl-triethoxysilane (APTS,  $\text{C}_9\text{H}_{23}\text{NO}_3\text{Si}$ , 99%), ammonium hydroxide ( $\text{NH}_3$  aq, 28%), sodium acetate ( $\text{NaOAc}$ , 99%),

ethylene glycol (EG,  $C_2H_6O_2$ , 99%), hydrochloric acid (HCl, 37%), ethyl acetate ( $C_4H_8O_2$ , 99.8%), 1-octadecene (ODE,  $C_{18}H_{36}$ , 90%), 2-propanol (IPA,  $C_3H_8O$ , 99.5%), cyclohexane (CHX,  $C_6H_{12}$ , 99.5%) and oleic acid (OA,  $C_{18}H_{34}O_2$ , 99%) were purchased from MERCK (Saint Louis, MO, USA). Ethanol ( $C_2H_5OH$ , absolute grade) was purchased from Panreac (Madrid, Spain). Phosphate-buffered saline (PBS) and high-glucose Dulbecco's modified Eagle's medium (DMEM) containing GlutaMax, fetal bovine serum (FBS), penicillin-streptomycin and trypsin were obtained from Gibco-Invitrogen (Gibco-Invitrogen™-Fisher, Carlsbad, CA, USA). Milli-Q (Millipore®, Burlington, MA, USA) deionized water was used in all the experiments.

## 2.2. Synthesis of MNPs

Depending on the synthesis route followed to produce the magnetic nanoprobe, single-core or multi-core structures can be obtained. In this work, magnetic cores were synthesized using bottom-up routes (co-precipitation, solvothermal and thermal decomposition methods), while the synthesis of core@shell MNPs were based on the Stöber and microemulsion methods. Surface modification with organic materials, like small fluorescent molecules (FITC or RITC), stabilizing agents (citrate or OA) or polymers (PDA, PEG or CS), and inorganic materials ( $SiO_2$ ) was used in this work in order to modulate surface ionic charge activity, improving colloidal stability and biocompatibility and providing specific physicochemical properties, such as optical abilities for bioimaging. The synthesis routes used to prepare different samples is compiled in Figure 1.

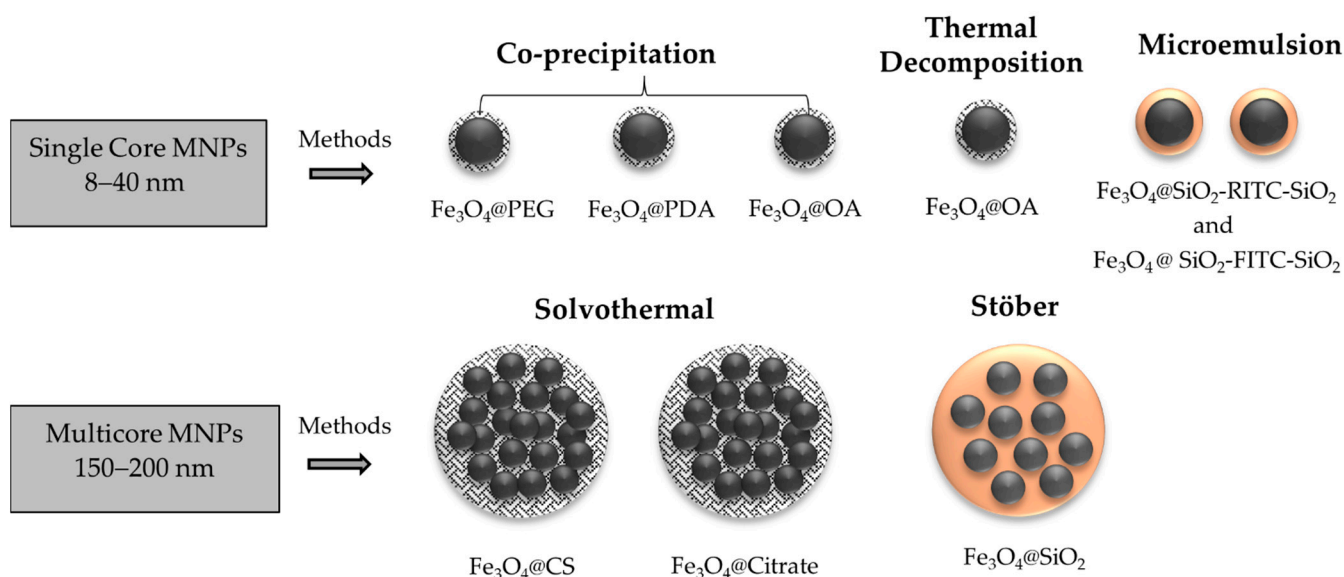


**Figure 1.** Schematic representation of the single-core MNPs synthesized by different methods—co-precipitation ( $Fe_3O_4@PEG$ ,  $Fe_3O_4@PDA$ ,  $Fe_3O_4@OA$ ), thermal decomposition ( $Fe_3O_4@OA$ ) and microemulsion ( $Fe_3O_4@SiO_2-RITC-SiO_2$  and  $Fe_3O_4@SiO_2-FITC-SiO_2$ )—and of the multi-core MNPs (down) synthesized by the solvothermal ( $Fe_3O_4@CS$  and  $Fe_3O_4@Citrate$ ) and Stöber ( $Fe_3O_4@SiO_2$ ) methods.

### 2.2.1. MNPs Prepared by Co-Precipitation Method

Polymer/stabilized-coated MNPs were obtained following Massart's procedure [50]. In a typical synthesis,  $FeCl_3 \cdot 6H_2O$  (45 mmol) and  $FeSO_4 \cdot 7H_2O$  (30 mmol) were dissolved in 100 mL of 10 mM HCl aqueous solution through mechanical stirring. The mixture was heated at 60 °C, then  $NH_3$  aq (770 mmol) and the desired biocompatible polymer or stabilizing agent (PDA, PEG or OA; 1.11 mmol) were added, and the reaction was carried out for 1 h. After that, the obtained MNPs were treated and washed differently depending on the hydrophilic/hydrophobic nature of their surface. Samples of  $Fe_3O_4$  coated with PDA or PEG were acidified up to pH 5 with the incorporation of the HCl

solution at 9%. Magnetite NPs were separated from the reaction medium by a magnetic field and washed several times with Milli-Q water. Finally, Fe<sub>3</sub>O<sub>4</sub>@PDA and Fe<sub>3</sub>O<sub>4</sub>@PEG MNPs were redispersed in Milli-Q water. Samples of Fe<sub>3</sub>O<sub>4</sub> nanoparticles coated with OA were transferred to a beaker and placed on a hot plate at 100 °C to allow flocculation. The precipitate containing Fe<sub>3</sub>O<sub>4</sub>@OA MNPs was separated from the reaction medium by a magnetic field and washed three times with Milli-Q water. Finally, Fe<sub>3</sub>O<sub>4</sub>@OA NPs were redispersed in CHX and the remaining water was completely removed from the organic phase by using a decantation funnel.

#### 2.2.2. MNPs Prepared by Thermal Decomposition Method

OA-coated MNPs (Fe<sub>3</sub>O<sub>4</sub>@OA) were prepared following Zhou's procedure [51]. Typically, iron-oleate complex (3 mmol) and OA (1.5 mmol) were added to a flask containing ODE (50 mL). After being filled with nitrogen atmosphere, the reaction mixture was heated at 320 °C at a constant heating rate of 6 °C min<sup>-1</sup> and then kept at that temperature for 120 min. MNPs were precipitated, magnetically separated and washed with ethanol (x4) and cyclohexane (x4). Finally, Fe<sub>3</sub>O<sub>4</sub>@OA NPs were resuspended in CHX.

#### 2.2.3. MNPs Prepared by Microemulsion Method

Fluorescent single core@shell silica MNPs were prepared according to a water in cyclohexane reverse microemulsion process [52,53], modified to incorporate the fluorescent molecule (FITC or RITC) into a silicate matrix and the silica coating on the MNPs through a four-stage method. In this case, Fe<sub>3</sub>O<sub>4</sub>@OA MNPs previously synthesized by co-precipitation and thermal decomposition methods were used as magnetic cores for the design of Fe<sub>3</sub>O<sub>4</sub>@SiO<sub>2</sub>-RITC-SiO<sub>2</sub> and Fe<sub>3</sub>O<sub>4</sub>@SiO<sub>2</sub>-FITC-SiO<sub>2</sub> MNPs, respectively, following a microemulsion procedure.

RITC (0.037 mmol) was dissolved in a sample vial (previously covered with aluminum foil to avoid damage of the fluorescent molecule during all the procedure) in deoxygenated ethanol (35 mL) and kept under magnetic stirring (200 rpm) for 30 min. After that, APTS (150 µL) was added to the mixture and left for 16 h under the same magnetic shaking conditions to facilitate the coupling completely. After 16 h of incubation, the solvent was evaporated to obtain a final mixture volume of 1 mL. The obtained fluorescent complex (APTS-FITC or APTS-RITC) was stored at a low temperature (4 °C) and protected from light by an aluminum foil envelope until further use.

In a typical synthesis, Fe<sub>3</sub>O<sub>4</sub>@OA NPs (10 mg dispersed in CHX), Igepal CO-520 (3.6 mmol) and cyclohexane (18.7 mL) were mixed in a sample vial and orbital shaken using an incubator for 30 min. Finally, the addition of NH<sub>3</sub> aq (210 µL) and the tetraethyl orthosilicate, TEOS, was added in three stages to the reaction and kept under the same orbital conditions during the entire procedure. First, TEOS (112 mmol) was added to the synthesis and left 2h, followed by the addition of the desired fluorescent complex (30 µL). After 1h of incubation, TEOS (56 mmol) was added to the mixture and left for 1 h to facilitate crosslinking. Finally, TEOS (56 mmol) was introduced to the solution and the reaction required a further 16h at room temperature to complete the silica coating. After that, IPA was added to precipitate the fluorescent single core@shell MNPs, which were magnetically separated and extensively washed with IPA (four times) and water (four times). Finally, the fluorescent single core@shell MNPs were redispersed in Milli-Q water.

#### 2.2.4. MNPs Prepared by Solvothermal Method

CS-coated multi-core MNPs (Fe<sub>3</sub>O<sub>4</sub>@CS) were obtained following Shen's procedure [54]. FeCl<sub>3</sub>·6H<sub>2</sub>O (5.6 mmol), CS (0.5 g), NaOAc (44 mmol) and PVP (1 g) were added to 70 mL of ethylene glycol to give a transparent solution via vigorous stirring. This mixture was then transferred to a 125 mL Teflon-lined autoclave for treatment at 200 °C for 8 h. The obtained multi-core Fe<sub>3</sub>O<sub>4</sub>@CS NPs were extensively washed with Milli-Q water and separated by magnetic decantation for several times. Finally, MNPs were redispersed in Milli-Q water.

Citrate-coated multi-core MNPs ( $\text{Fe}_3\text{O}_4\text{@Citrate}$ ) were prepared as reported by Jiang et al. [55]. Briefly,  $\text{FeCl}_3 \cdot 6\text{H}_2\text{O}$  (3.75 mmol) and sodium citrate (0.4 mmol) were dissolved in EG (30 mL) under magnetically stirring (200 rpm) for 30 min. Then, NaOAc (33 mmol) was added and kept under magnetically stirring until it was totally dissolved. The solution was transferred to a 45 mL Teflon-lined autoclave, which was sealed and maintained at 200 °C for 15 h. After the reaction, the autoclave was allowed to cool down to room temperature naturally. The obtained multi-core  $\text{Fe}_3\text{O}_4\text{@Citrate}$  MNPs were washed with Milli-Q water and ethanol several times and then redispersed in Milli-Q water.

#### 2.2.5. MNPs Prepared by Stöber Method

Multi-core@shell silica MNPs ( $\text{Fe}_3\text{O}_4\text{@SiO}_2$ ) were synthesized following Mohammad's procedure [56], with some modifications. In this section, the TEOS precursor was used for seed-mediated growth of silica on the surface of previously synthesized magnetite nanoparticles functionalized with PEG by the co-precipitation method [50]. First, 1 mL of  $\text{Fe}_3\text{O}_4\text{@PEG}$  (3.5 mg/mL) was dispersed in ethanol (5 mL) with a sonication bath for 15 min to ensure adequate dispersion. Then,  $\text{NH}_3$  aq (114.6  $\mu\text{L}$ ) and TEOS (100  $\mu\text{L}$ ) were added to the mixture and orbitally stirred using an incubator at room temperature for 24 h. Afterwards, the multi-core@shell MNPs were magnetically separated, washed and redispersed in Milli-Q water.

### 2.3. Physicochemical Characterization

#### 2.3.1. XRD Structural Characterization

The characterization of the crystalline phases was performed by X-ray diffraction (XRD) with powder samples using a Philips PW1710 diffractometer (Panalytical, Brighton, UK) with a  $\text{Cu K}\alpha$  radiation source,  $\lambda = 1.54186 \text{ \AA}$ . Measurements were collected in the  $2\theta$  angle range between 10° and 80° with steps of 0.02° and 10 s/step. The peak broadening of XRD patterns was used to obtain crystallite size using Scherrer's equation [57]:

$$d = \frac{k\lambda}{\beta \cos \theta_{\text{hkl}}} \quad (1)$$

where  $d$  is the mean size of the crystallite (nm),  $k$  is the Scherrer constant (0.9, dimensionless),  $\lambda$  is the wavelength of the X-ray beam used (0.154060 nm),  $\beta$  is the full width at half maximum (FWHM, radians) of the peak and  $\theta$  is the Bragg angle (degrees).

#### 2.3.2. Microscopy Morphological Characterization

The morphology and size of the MNPs were studied by transmission electron microscopy (TEM) using a JEOL JEM-1011 microscope operating at 100 kV (JEOL, Tokyo, Japan). Samples were placed on copper grids with Formvar<sup>®</sup> films for analysis. The Image J program (distributed by NIH, USA) was used to measure the diameters of the MNPs.

#### 2.3.3. Surface Chemistry Characterization

Fourier transform infrared (FTIR) spectra of the surface functional groups of the nanostructures were recorded with a Thermo Nicolet Nexus spectrometer (Thermo Fisher Scientific, Madrid, Spain) using the attenuated total reflectance (ATR) method from 4000 to 400  $\text{cm}^{-1}$ .

#### 2.3.4. Hydrodynamic Particle Size and Zeta Potential Measurements

Measurements of hydrodynamic particle size and  $\zeta$ -Potential of MNPs were routinely performed on the same instrument by a Zetasizer Nano ZS (Malvern Instruments, Worcestershire, UK) equipped with a He-Ne laser (633 nm) and operating at a scattering angle of 173° and at room temperature. All analysis were performed in triplicate. All multi-functional magnetic nanoprobe were dispersed in Milli-Q water with an iron or magnetic material concentration of 0.4 mg/mL (approx.) and at pH 6.5.

Zeta potential measurements were carried out using a Malvern Nano ZS instrument (Malvern Instruments, Worcestershire, UK) supplied by DTS Nano V7.11 software (Malvern Instruments, Worcestershire, UK) when the functionalized nanoprobe were dispersed in Milli-Q water with an iron or magnetic material concentration of 0.4 mg/mL (approx.) and at pH 6.5. The Smoluchowski equation was used for zetametry measurements.

#### 2.3.5. Compositional Characterization

The iron content of the MNPs samples was determined by flame atomic absorption spectroscopy (FAAS) performed with an Atomic Absorption Spectrometer (Perkin Elmer, Waltham, MA, USA).

The composition of the samples was analyzed with a TGA Perkin Elmer model 7 (Perkin Elmer, Waltham, MA, USA).

#### 2.3.6. Optical Properties

The optical properties were measured using a Fluorescent Spectrophotometer (Varian Cary Eclipse).

Additionally, fluorescent MNPs imaging was performed with a fluorescence confocal multispectral imaging Confocal Laser microscope Leica TCS SP8 SMD. Technical specifications: resolution,  $1024 \times 1024$ ; scan direction X, bidirectional; objective, HC PL APO CS  $63 \times /1.40$  OIL, using the 405 nm, 488 nm and 552 nm laser lines to PDA, FTIC and RITC fluorescent visualization, respectively.

Cell micrographs were imaged in a Leica DMI 6000 B microscope with the software LAS AF 1.0.0 (Leica Microsystems, Wetzlar, Germany).

#### 2.3.7. DC Magnetic Characterization

Direct current (DC) magnetization curves of dried samples were measured using a vibrating sample magnetometer (VSM) (DMS, Lowell, MA, USA). In such a device, the measurement of magnetic hysteresis loops at room temperature was carried out under external magnetic fields from  $-10$  to  $10$  kOe. Temperature dependence measurements of the MNPs magnetization were made in field-cooled (FC) and zero-field-cooled (ZFC) conditions using a Superconducting Quantum Interference Device (SQUID) Magnetometer (Quantum Design, Darmstadt, Germany).

#### 2.3.8. AC Magnetic Characterization

AC magnetometry measurements were performed using a commercial inductive magnetometer (AC Hyster Series; Nanotech Solutions, Madrid, Spain) with the application of a magnetic field of  $20 \text{ kAm}^{-1}$  at a frequency of 200, 250, 300 and 350 kHz.

#### 2.3.9. Magnetic Hyperthermia Characterization

Magnetic hyperthermia response of MNPs was measured using a commercially available setup (MagneTherm, Nanotherics, Warrington, UK) equipped with a fiber optic, operating at a fixed magnetic field of  $20 \text{ kAm}^{-1}$  and different frequencies.

### 3. Results and Discussion

#### 3.1. X-ray Diffraction (XRD)

To determine the crystalline phases of the MNPs, X-ray diffraction was used, and powder X-ray patterns of all samples are shown in Figure 2. Diffractograms of fluorescent single-core MNPs ( $\text{Fe}_3\text{O}_4@PDA$ ,  $\text{Fe}_3\text{O}_4@SiO_2\text{-FITC-SiO}_2$  and  $\text{Fe}_3\text{O}_4@SiO_2\text{-RITC-SiO}_2$ ) and multi-core MNPs ( $\text{Fe}_3\text{O}_4@SiO_2$ ,  $\text{Fe}_3\text{O}_4@CS$  and  $\text{Fe}_3\text{O}_4@Citrate$ ) are shown in Figure 2a,b, respectively. The XRD characterization of the magnetic cores composed of  $\text{Fe}_3\text{O}_4@OA$  and  $\text{Fe}_3\text{O}_4@PEG$  MNPs, corresponding to  $\text{Fe}_3\text{O}_4@SiO_2\text{-FITC-SiO}_2$ ,  $\text{Fe}_3\text{O}_4@SiO_2\text{-RITC-SiO}_2$  and multi-core  $\text{Fe}_3\text{O}_4@SiO_2$  is shown in Figure S1. The diffraction peaks of all MNPs match the theoretical diffraction peaks at  $(1\ 1\ 1)$ ,  $(2\ 2\ 0)$ ,  $(3\ 1\ 1)$ ,  $(4\ 0\ 0)$ ,  $(4\ 2\ 2)$ ,  $(5\ 1\ 1)$ ,  $(4\ 4\ 0)$ ,  $(6\ 2\ 0)$  and  $(5\ 5\ 3)$ , corresponding to the inverse spinel structure crystalline phase of magnetite from

the Inorganic Crystal Structure Database (ICSD card No. 98-015-8742) [58]. However, the presence of other iron oxide phases, such as maghemite, cannot be discarded. It is worth noting the presence of peaks corresponding to the functional inorganic coatings of the MNPs, as in the case of fluorescent single-core@shell and multi-core@shell ( $\text{Fe}_3\text{O}_4@SiO_2$ -FITC- $SiO_2$ ,  $\text{Fe}_3\text{O}_4@SiO_2$ -RITC- $SiO_2$  and  $\text{Fe}_3\text{O}_4@SiO_2$ ) with a broad band located between  $15^\circ$ – $30^\circ$ , indicating the amorphous nature of silica shell [59]. In addition, a broad band located at  $18^\circ$  is observed in the multi-core  $\text{Fe}_3\text{O}_4@CS$  pattern, which corresponds to the chitosan coating [60]. The crystallite size of single-core and multi-core MNPs, compiled in Table 1, was calculated using Scherrer's equation, Equation (1) and applied to the most intense peak (311). The crystallite sizes are almost the same or slightly smaller than the particle sizes, indicating that each particle consists of a single crystal.

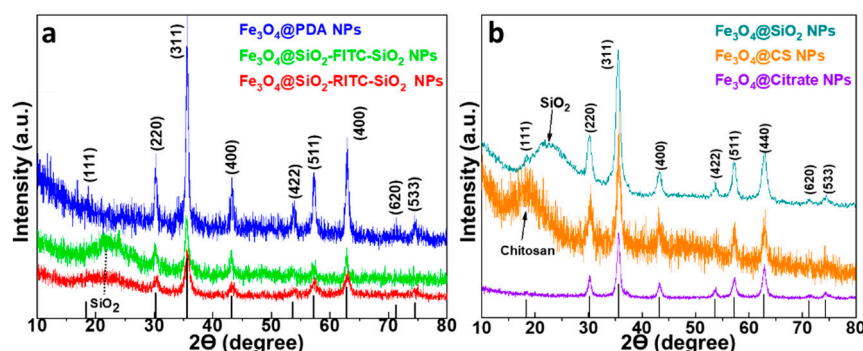


**Figure 2.** XRD patterns of (a) single-core MNPs,  $\text{Fe}_3\text{O}_4@PDA$  (blue pattern),  $\text{Fe}_3\text{O}_4@SiO_2$ -FITC- $SiO_2$  (green pattern) and  $\text{Fe}_3\text{O}_4@SiO_2$ -RITC- $SiO_2$  (red pattern), and (b) multi-core MNPs,  $\text{Fe}_3\text{O}_4@SiO_2$  (dark cyan pattern),  $\text{Fe}_3\text{O}_4@CS$  (orange pattern) and  $\text{Fe}_3\text{O}_4@Citrate$  (violet pattern), compared to the XRD pattern of magnetite from the ICSD card No. 98-015-8742 data base.

**Table 1.** Non-magnetic content, hydrodynamic size ( $D_H$ ), crystal size obtained by XRD characterization ( $D_{XRD}$ ), TEM size obtained by TEM micrographs ( $D_{TEM}$ ), polydispersity index (PDI) and zeta potential.

Core	Coating	Layer Content (wt %)	$D_H$ (nm)	$D_{XRD}$ (nm)	$D_{TEM}$ (nm)	PDI	Zeta Potential (mV)
Single-Core	PDA	41.70	$163.00 \pm 131.50$	12.27	14.90	0.445	(+) 28.70
	$SiO_2$ -RITC	75.10	$44.14 \pm 19.73$	9.28	22.50	0.195	(−) 38.00
	$SiO_2$ -FITC	82.60	$142.20 \pm 50.47$	8.59	40.09	0.265	(−) 45.50
Multi-Core	CS	34.10	$201.20 \pm 52.56$	13.04	178.44	0.259	(+) 12.00
	Citrate	7.10	$339.80 \pm 218.00$	13.25	145.96	0.233	(−) 50.50
	$SiO_2$	78.1	$215.50 \pm 61.91$	9.82	197.27	0.146	(−) 45.93

The FTIR spectra, presented in Figure 3a for the single-core MNPs and Figure 3b for the multi-core MNPs, were used to assess the effective surface functionalization through the absorption bands. FTIR spectra of all samples show similar absorption bands at  $3400\text{ cm}^{-1}$ , which is characteristic peak to the presence of hydroxyl groups from the adsorbed water molecules and attributed to O-H stretching [61], and at around  $550\text{ cm}^{-1}$ , associated with the stretching vibration of the tetrahedral groups ( $\text{Fe}^{3+}-\text{O}^{2-}$ ) for  $\text{Fe}_3\text{O}_4$  [62]. For PDA coated  $\text{Fe}_3\text{O}_4$  MNPs, the bands located at  $3358$ ,  $2919$ ,  $2857$ ,  $1610$ ,  $1431$  and  $1290\text{ cm}^{-1}$ , associated at -NH stretching, - $\text{CH}_2$  (asymmetric and symmetric), -C-N stretching, -NH bending and -C-N-C stretching vibrations, respectively [63]. For single- and multi-core@shell MNPs FTIR spectra, silica coating can be confirmed by the appearance of three peaks at around  $1050$ ,  $4793$  and  $463\text{ cm}^{-1}$ , corresponding to the stretching modes of Si-O-Si (asymmetric and symmetric) and the scissoring vibration of Si-O-Si, respectively [64]. Chitosan-coated  $\text{Fe}_3\text{O}_4$  NPs show a weak peak at  $3377$  and  $1610\text{ cm}^{-1}$  associated to the presence of amine groups (-NH stretching and -NH bending vibrations, respectively). The absorptions band at  $2923$ ,

2862  $\text{cm}^{-1}$  are correlated to the asymmetric and symmetric  $\text{CH}_2$  stretching of copolymer chitosan, respectively. In addition, two peaks appear around 1410 and 1034  $\text{cm}^{-1}$ , which prove the presence of the amide group of chitosan (C-N and C-O-C stretching vibrations, respectively). Moreover, citrate-coated  $\text{Fe}_3\text{O}_4$  FTIR spectra demonstrated the correct citrate coating by the presence of clearly observed absorptions bands at 1373, 1367 and 1060  $\text{cm}^{-1}$ , which are attributed to the stretching mode (asymmetric  $\text{COO}^-$ , symmetric  $\text{COO}^-$  and  $-\text{CH}_2$ , respectively) groups of citrates [64]. The FTIR characterization of the magnetic cores composed of  $\text{Fe}_3\text{O}_4@OA$  and  $\text{Fe}_3\text{O}_4@PEG$  MNPs, corresponding to  $\text{Fe}_3\text{O}_4@SiO_2\text{-FITC-SiO}_2$ ,  $\text{Fe}_3\text{O}_4@SiO_2\text{-RITC-SiO}_2$  and multi-core  $\text{Fe}_3\text{O}_4@SiO_2$  is shown in Figure S2.

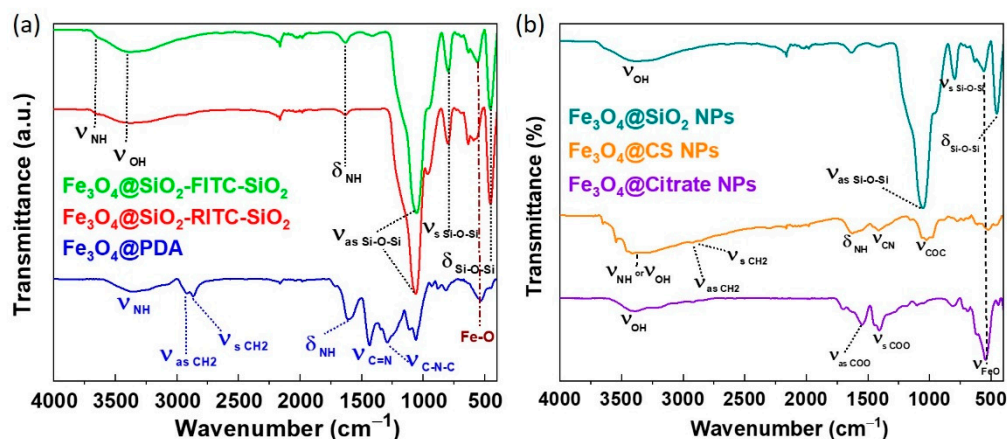


**Figure 3.** FTIR spectra of (a) single-core MNPs,  $\text{Fe}_3\text{O}_4@PDA$  (blue pattern),  $\text{Fe}_3\text{O}_4@SiO_2\text{-FITC-SiO}_2$  (green pattern) and  $\text{Fe}_3\text{O}_4@SiO_2\text{-RITC-SiO}_2$  (red pattern), and (b) multi-core MNPs,  $\text{Fe}_3\text{O}_4@SiO_2$  (dark cyan pattern),  $\text{Fe}_3\text{O}_4@CS$  (orange pattern) and  $\text{Fe}_3\text{O}_4@Citrate$  (violet pattern).

### 3.2. Transmission Electron Microscopy (TEM)

The morphology and size of iron oxide MNPs, characterized by TEM micrographs, are shown in Figures 4 and 5 for single-core and multi-core MNPs, respectively. All MNPs show a quasi-spherical morphology and sizes, compiled in Table 1, between 14.90 nm ( $\text{Fe}_3\text{O}_4@PDA$  NPs) and 197.30 nm ( $\text{Fe}_3\text{O}_4@SiO_2$  multi-core MNPs). Regarding the single-core MNPs, from these images it was possible to observe a higher agglomeration in the MNPs synthesized by the coprecipitation method ( $\text{Fe}_3\text{O}_4@PDA$ ), compared to the MNPs synthesized by the microemulsion method ( $\text{Fe}_3\text{O}_4@SiO_2\text{-RITC-SiO}_2$  and  $\text{Fe}_3\text{O}_4@SiO_2\text{-FITC-SiO}_2$ ), where magnetite cores (dark contrast) are individually embedded within the silica (light contrast) with averaged size of 22.50 nm and 40.09 nm, respectively. On the other hand, the TEM images of the multi-core MNPs revealed particle sizes an order of magnitude larger than the single-core MNPs:  $\text{Fe}_3\text{O}_4@CS$  (178.44 nm),  $\text{Fe}_3\text{O}_4@Citrate$  (145.96 nm) and  $\text{Fe}_3\text{O}_4@SiO_2$  (197.27 nm). A clear structure formed by small magnetic cores was observed in the MNPs synthesized by the solvothermal method  $\text{Fe}_3\text{O}_4@CS$  (Figure 5a) and  $\text{Fe}_3\text{O}_4@Citrate$  (Figure 5b) and, for multi-core  $\text{Fe}_3\text{O}_4@SiO_2$  MNPs synthesized by Stöber method (Figure 5c), a core@shell structure formed by the clustering of small MNPs covered by a thick  $\text{SiO}_2$  shell with spherical shape can be observed.

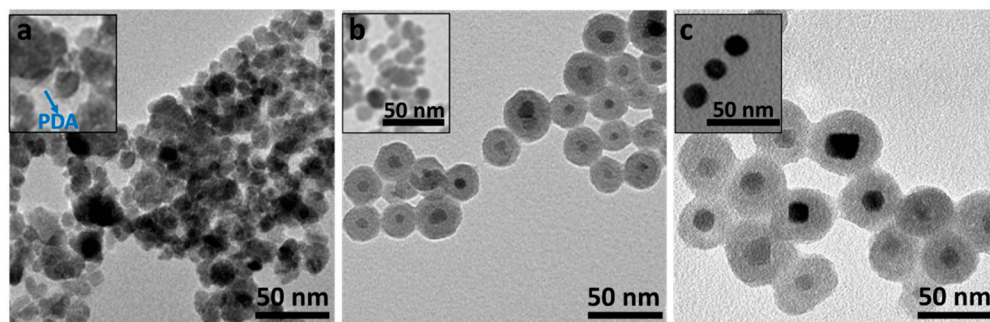


**Figure 4.** Representative TEM micrographs of the fluorescent MNPs: single-core  $\text{Fe}_3\text{O}_4$ @PDA (a), single-core@shell  $\text{Fe}_3\text{O}_4$ @ $\text{SiO}_2$ -RITC- $\text{SiO}_2$  (b),  $\text{Fe}_3\text{O}_4$ @ $\text{SiO}_2$ -FITC- $\text{SiO}_2$  (c). Insets of (a) show a zoom of the  $\text{Fe}_3\text{O}_4$ @PDA TEM micrographs and (b,c) magnetic cores prior to silica coating.

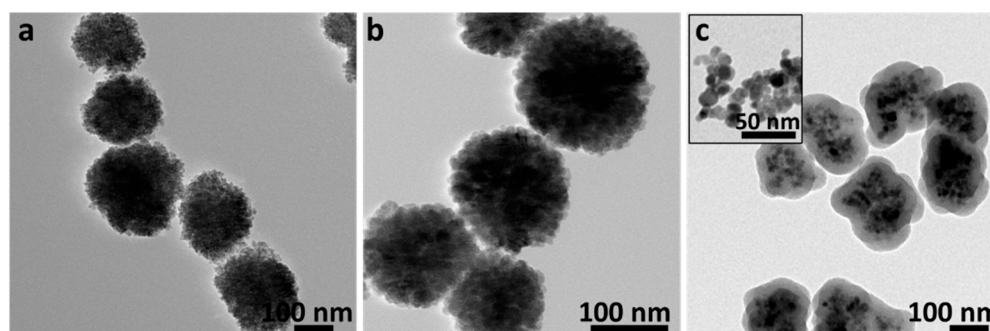


**Figure 5.** Representative TEM micrographs of the multi-core MNPs:  $\text{Fe}_3\text{O}_4$ @CS (a),  $\text{Fe}_3\text{O}_4$ @Citrate (b) and the core@shell  $\text{Fe}_3\text{O}_4$ @ $\text{SiO}_2$  (c). Insets show magnetic cores prior to silica coating.

Thermogravimetry and FAAS analyses allowed the quantification of the amount of organic and inorganic content, respectively, contained in each MNPs. In this way, different values of the %w of the shell content, compiled in Table 1, were obtained, depending on the synthesis, with the multi-core  $\text{Fe}_3\text{O}_4$ @Citrate MNPs being the ones with the lowest percentage of organic content (7.14%) and the single-core  $\text{Fe}_3\text{O}_4$ @ $\text{SiO}_2$ -FITC MNPs the ones with the highest content (82.60%). Regarding the single-core MNPs,  $\text{Fe}_3\text{O}_4$ @PDA MNPs have the lowest organic content (41.70%) compared to the highest values revealed for  $\text{Fe}_3\text{O}_4$ @ $\text{SiO}_2$ -RITC (75.1%) MNPs. On the other hand,  $\text{Fe}_3\text{O}_4$ @CS present a higher percentage of organic content (34.12%) than multi-core  $\text{Fe}_3\text{O}_4$ @Citrate (7.14%) synthesized by the solvothermal method but much lower values than  $\text{Fe}_3\text{O}_4$ @ $\text{SiO}_2$  multi-core MNPs (78.10%) synthesized by the Stöber method.

The colloidal stability of single- and multi-core MNPs was evaluated by hydrodynamic size and zeta potential analysis (Table 1). DLS measurements revealed that the fluorescent single core@shell ( $\text{Fe}_3\text{O}_4$ @ $\text{SiO}_2$ -RITC- $\text{SiO}_2$ ) MNPs possess a relatively small hydrodynamic diameters, close to the particle size and their zeta potential ( $-45.50$  mV), and PDI (0.195) indicates that the MNPs are stable and that the nanoparticle size distribution is relatively uniform compared to the single-core  $\text{Fe}_3\text{O}_4$ @PDA MNPs, where their PDI, greater than 0.4, indicates a moderate aggregation of the MNPs in aqueous medium [65] and its positive zeta potential ( $+28.70$  mV) indicates the correct functionalization with PDA of the entire surface of the MNPs [66]. On the other hand, the PDI values of multi-core MNPs are lower than 0.4, which indicates a good dispersion in aqueous solution. From the results of zeta potential, listed in Table 1, it was found that the surfaces of CS-coated MNPs have positive charges ( $+12$  mV), which is common due to the cationic characteristic of CS [67]. Moreover, negative charges were found in the surfaces of multi-core MNPs ( $\text{Fe}_3\text{O}_4$ @Citrate and  $\text{Fe}_3\text{O}_4$ @ $\text{SiO}_2$ ), indicating the presence of carboxylic acid groups and silanol groups from citrate and silica layers, respectively [68,69].

### 3.3. Optical Characterization of Fluorescent Single-Core MNPs

The optical characterization of the fluorescent activity of PDA- ( $\text{Fe}_3\text{O}_4@\text{PDA}$ ), FITC- ( $\text{Fe}_3\text{O}_4@\text{SiO}_2\text{-FITC-SiO}_2$ ) and RITC ( $\text{Fe}_3\text{O}_4@\text{SiO}_2\text{-RITC-SiO}_2$ )-functionalized MNPs, observed in Figure 6, reveals well-defined peaks, both excitation and emission, with maxima located at 424 nm ( $\text{Fe}_3\text{O}_4@\text{PDA}$ ), 515 nm ( $\text{Fe}_3\text{O}_4@\text{SiO}_2\text{-FITC-SiO}_2$ ) and 583 nm ( $\text{Fe}_3\text{O}_4@\text{SiO}_2\text{-RITC-SiO}_2$ ) agreeing with those reported theoretically for each fluorophore [70–72]. To verify whether fluorescent single-core MNPs have a sufficient response to be used in microscopy images for biological studies, these were analyzed by confocal microscopy using laser excitation lines of 405, 488 and 522 nm, showing the images in Figure 6d,e, respectively, and allowing the visualization of PDA, FITC and RITC, respectively.

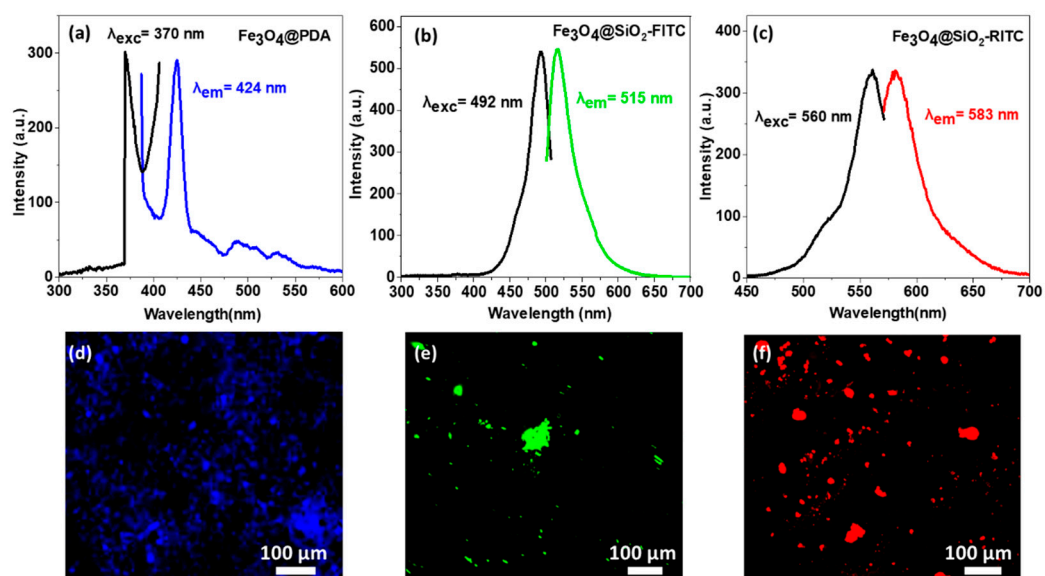


**Figure 6.** Photoluminescence spectra and confocal fluorescence microscope images of the fluorescent single-core MNPs, functionalized with fluorescent agent: PDA (a,d), FITC (b,e) and RITC (c,f), respectively.

### 3.4. Magnetic Characterization

To characterize the DC magnetic properties of the single core and multi-core MNPs, hysteresis loops, presented in Figure 7a,b, respectively, were performed at 300 K using a magnetic field between  $-10$  and  $10$  kOe with a VSM magnetometer. The insets show the low-field region in more detail, where the coercivity ( $H_C$ ) and remanence ( $M_R$ ) of MNPs, compiled in Table 2, can be observed. The saturation magnetization ( $M_S$ ) values obtained in single core MNPs differ from one MNP to another. On the one hand, the MNPs synthesized by the coprecipitation method,  $\text{Fe}_3\text{O}_4@\text{PDA}$  and  $\text{Fe}_3\text{O}_4@\text{SiO}_2\text{-RITC-SiO}_2$  (formed by  $\text{Fe}_3\text{O}_4@\text{OA}$  magnetic core) MNPs, present similar  $M_S$  values,  $65\text{--}70$   $\text{emu g}^{-1}$ ; while  $\text{Fe}_3\text{O}_4@\text{SiO}_2\text{-FITC-SiO}_2$  MNPs, (produced from  $\text{Fe}_3\text{O}_4@\text{OA}$  magnetic core by thermal decomposition method) show a reduced saturation magnetization around  $M_S = 50$   $\text{emu g}^{-1}$ . Regarding the MNPs produced with magnetic cores obtained from coprecipitation methods, the obtained  $M_S$  values are in the range of what is expected for this type of synthesis previously reported. However, the difference of about  $5$   $\text{emu/g}$  between both ( $\text{Fe}_3\text{O}_4@\text{PDA}$  and  $\text{Fe}_3\text{O}_4@\text{SiO}_2\text{-RITC-SiO}_2$ ) can be ascribed to the effect of the coating material added in the synthesis (PDA and OA) that may modify the growth of the MNPs. On the other hand, the lower  $M_S$  of  $\text{Fe}_3\text{O}_4@\text{SiO}_2\text{-FITC-SiO}_2$ , whose core was synthesized by the thermal decomposition method, agrees with the results reported for MNPs obtained through this type synthesis and is ascribed to the spin-canting effect on the surface of the MNPs that considerably reduces the  $M_S$  [51]. This does not occur in the multi-core MNPs which, despite being formed by different methods, present similar  $M_S$  values:  $\text{Fe}_3\text{O}_4@\text{CS}$  ( $M_S = 67.35$   $\text{emu g}^{-1}$ ),  $\text{Fe}_3\text{O}_4@\text{Citrate}$  ( $M_S = 67.45$   $\text{emu g}^{-1}$ ) and  $\text{Fe}_3\text{O}_4@\text{SiO}_2$

( $M_S = 67.05 \text{ emu g}^{-1}$ ). The magnetization values obtained were lower than the value of bulk magnetite ( $M_S^{\text{bulk}} = 92 \text{ emug}^{-1}$ ) [73], which is concordance to the surface dead magnetic layer of magnetic nanoparticles that reduces their magnetization [74]. However, although the  $M_S$  values were revealed to be similar in the multi-core MNPs, differences are observed in the magnetization curves. The main difference is observed in the high-field region of the hysteresis loop, where the saturation process starts to be seen. For  $\text{Fe}_3\text{O}_4@SiO_2$  MNPs, a steeper slope was observed, as was a less clear saturation (flattening of the curve), than in  $\text{Fe}_3\text{O}_4@CS$  and  $\text{Fe}_3\text{O}_4@Citrate$ . This phenomenon hints at a slightly higher paramagnetic contribution to the hysteresis loop that is related to a larger size of the spin dead layer [75]. This difference may be due to the different synthesis methods used to produce multi-core MNPs. While  $\text{Fe}_3\text{O}_4@CS$  and  $\text{Fe}_3\text{O}_4@Citrate$  were synthesized at high temperatures (above  $200 \text{ }^\circ\text{C}$ ) and present a large particle size (150–200 nm),  $\text{Fe}_3\text{O}_4@SiO_2$  MNPs were formed by  $\text{Fe}_3\text{O}_4@PEG$  magnetic cores, previously synthesized by the coprecipitation method at lower temperatures ( $60 \text{ }^\circ\text{C}$ ) and with a smaller size (10 nm). These may suggest that  $\text{Fe}_3\text{O}_4@CS$  and  $\text{Fe}_3\text{O}_4@Citrate$  MNPs have a better crystalline structure with magnetite/maghemite crystals in purer composition, which is reflected in the lower paramagnetic contribution in the hysteresis loops.

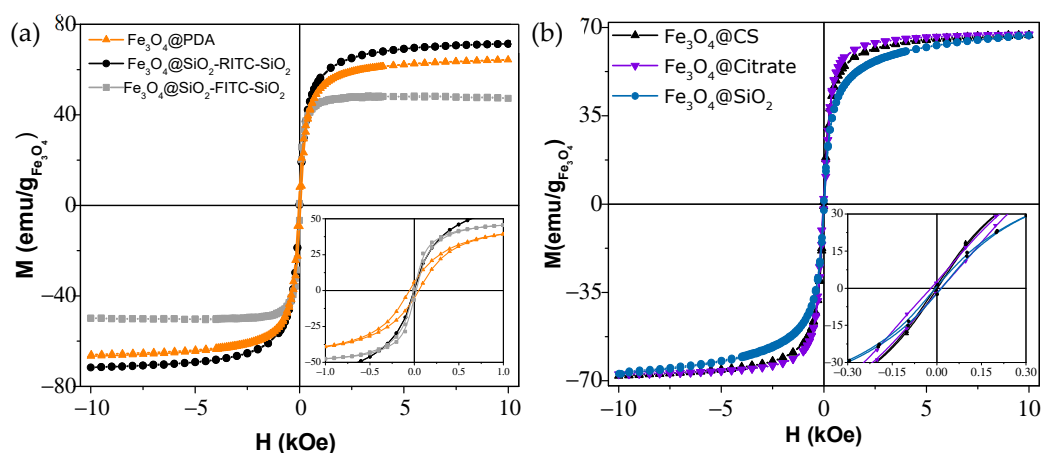


**Figure 7.** Magnetization curves at room temperature for the single-core (a) MNPs,  $\text{Fe}_3\text{O}_4@PDA$  (orange triangle),  $\text{Fe}_3\text{O}_4@SiO_2\text{-RITC-SiO}_2$  (black dots) and  $\text{Fe}_3\text{O}_4@SiO_2\text{-FITC-SiO}_2$  (gray dots), and multi-core (b) MNPs,  $\text{Fe}_3\text{O}_4@CS$  (black triangles),  $\text{Fe}_3\text{O}_4@Citrate$  (purple triangles) and  $\text{Fe}_3\text{O}_4@SiO_2$  (blue dots).

**Table 2.** Saturation magnetization ( $M_S$ ), coercivity ( $H_C$ ), remanence ( $M_R$ ) and blocking temperature ( $T_B$ ) obtained by DC magnetometry.

	Coating	$M_S$ ( $\text{emug}^{-1}$ )	$M_R$ ( $\text{emug}^{-1}$ )	$H_C$ (Oe)	$T_B$ (K)
Single-Core	PDA	65.38	5.74	51.7	>350
	$SiO_2\text{-RITC}$	71.44	0.65	3.53	96
	$SiO_2\text{-FITC}$	49.89	3.35	13.45	216
Multi-Core	CS	67.35	0.70	3.85	>350
	Citrate	67.45	2.33	17.19	>350
	$SiO_2$	67.05	1.44	10.18	~350

On the other hand, the coercivity values are close to zero for all MNPs ( $H_C > 20$  Oe), except for  $\text{Fe}_3\text{O}_4@PDA$  MNPs, whose coercivity increases up to 50 Oe, probably due to the larger nanoparticle size ( $D_{\text{TEM}} = 14.9 \text{ nm}$ ). The same behavior is observed in the remanence values where  $\text{Fe}_3\text{O}_4@PDA$  MNPs present the highest remanence value ( $M_R = 5.34 \text{ emu g}^{-1}$ ).

The temperature dependence of the magnetization, presented in Figure 8, was obtained by the ZFC-FC measurements from very low temperature (10 K) to room tempera-

ture (350 K), revealing clearly differentiated behaviors. Regarding the single core MNPs, observed in Figure 8a, the  $\text{Fe}_3\text{O}_4@PDA$  MNPs (orange line) do not exhibit superparamagnetic behavior at room temperature, while the  $\text{Fe}_3\text{O}_4@SiO_2\text{-RITC-SiO}_2$  (gray line) and  $\text{Fe}_3\text{O}_4@SiO_2\text{-FITC-SiO}_2$  (black line) MNPs exhibit blocking temperatures, obtained as the maximum of the ZFC curve, of 96 K and 216 K, respectively, showing superparamagnetic behavior at room temperature. On the other hand, ZFC-FC curves of multi-core  $\text{Fe}_3\text{O}_4@CS$  (black line) and  $\text{Fe}_3\text{O}_4@Citrate$  (purple line) MNPs, presented in Figure 8b, synthesized by the solvothermal method, reveal  $T_B$  that is higher than 350 K, while in multi-core  $\text{Fe}_3\text{O}_4@SiO_2$  MNPs (blue line), the corresponding  $T_B$  is around 350 K. These results suggest that magnetic interaction effects noticeably affect the overall behavior of the MNPs when they are agglomerated in a powder state to carry on measurements. Therefore, the use of functional  $\text{SiO}_2$  coatings in the  $\text{Fe}_3\text{O}_4@SiO_2\text{-FITC-SiO}_2$  and  $\text{Fe}_3\text{O}_4@SiO_2\text{-RITC-SiO}_2$  single-core MNPs and in the  $\text{Fe}_3\text{O}_4@SiO_2$  multi-core MNPs avoids the direct interaction between the magnetic cores, acting as spacers, and ensures the superparamagnetic behavior observed in these MNPs [76]. On the other hand, for the multi-core MNPs synthesized by solvothermal method, formed by small grouped MNPs, the interaction effects are strong and superparamagnetic behavior is inhibited.

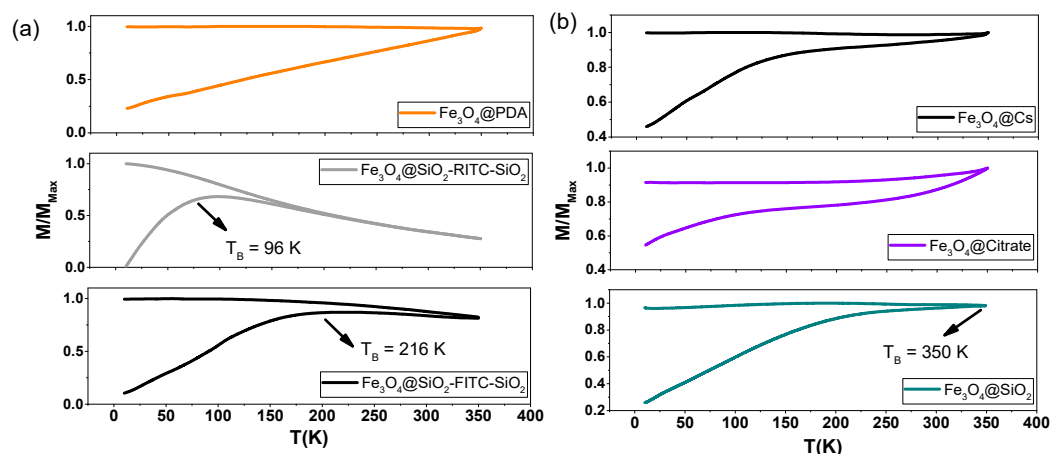


**Figure 8.** Zero-field-cooled (ZFC) and field-cooled (FC) measurements of (a) single core MNPs,  $\text{Fe}_3\text{O}_4@PDA$  (orange line),  $\text{Fe}_3\text{O}_4@SiO_2\text{-RITC-SiO}_2$  (gray line) and  $\text{Fe}_3\text{O}_4@SiO_2\text{-FITC-SiO}_2$  (black line), and (b) multi-core MNPs,  $\text{Fe}_3\text{O}_4@CS$  (black line),  $\text{Fe}_3\text{O}_4@Citrate$  (purple line) and  $\text{Fe}_3\text{O}_4@SiO_2$  (blue line).

### 3.5. Magnetic Uptake and Cell Isolation with Fluorescence Single-Core MNPs

Single core MNPs with fluorescent properties were tested as multifunctional tools for the magnetic isolation of living cells using A HeLa cell line (ATCC<sup>®</sup> CCL-2<sup>™</sup>), as presented in Figure 9a. Cells were maintained in DMEM (Dulbecco's modified Eagle's medium) containing 10% fetal bovine serum and 1% penicillin/streptomycin and were cultured with this complete medium under a humidified atmosphere containing 95% air and 5% of  $\text{CO}_2$  at 37 °C. Next, MNPs were poured over the cells and a transfection process stimulated by the presence of external permanent magnets located underneath the culture plates was carried out with the aim of boosting the cellular uptake procedure [77]. For this, cells were seeded at a density of  $10^4$  cells/well in a 12 plate and were incubated at 37 °C containing 95% air and 5%  $\text{CO}_2$  for 24 h. Then, 50  $\mu\text{L}$  of fluorescence MNPs (100  $\mu\text{g}/\text{mL}$ ) were inoculated after 24 h with 80% confluency incubated for 15 min with a magnetic plate under the 12 well plate. After this time wells were washed with PBS to eliminate nanoparticle remains and medium to then trypsinize it.

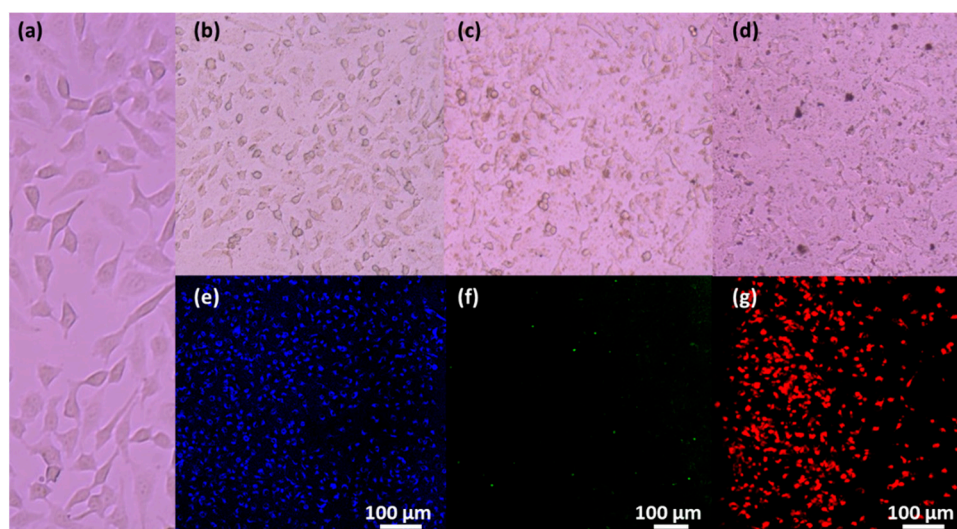


**Figure 9.** Microscope images of (a) HeLa control cells and magnetic uptake (up) and confocal fluorescence micrographs (dow) of fluorescent single-core MNPs, functionalized with fluorescent agent: PDA (b,e), FITC (c,f) and RITC (d,g), respectively.

Afterwards, to test the magnetic cell isolation procedure, cells were detached and moved to a 15 mL tube. Then, with the help of an external magnetic field, cells transfected with magnetic nanoparticles were separated from non-transfected cells. The supernatant was discarded, and “magnetized” cells were seeded again in other plate. For the observation of the isolated cells a fluorescence microscope (Zeiss Axio Scope A1, Oberkochen, Germany) was used to check uptake efficiency of the fluorescent tagging with the single-core MNPs, allowing the demonstration of the correct separation by means of external magnetic fields.

Figure 9 shows the micrographs corresponding to the magnetic uptake of the MNPs by the cells after 15 min of incubation and the corresponding fluorescence images of the MNPs internalized in the HeLa cells, where the emissions corresponding to the different fluorescent entities can be observed:  $\text{Fe}_3\text{O}_4$ @PDA (Figure 9b,e),  $\text{Fe}_3\text{O}_4$ @ $\text{SiO}_2$ -FITC- $\text{SiO}_2$  (Figure 9c,f) and  $\text{Fe}_3\text{O}_4$ @ $\text{SiO}_2$ -RITC- $\text{SiO}_2$  (Figure 9d,g). Through fluorescence images, it can be observed that the magnetic internalization efficiency using  $\text{Fe}_3\text{O}_4$ @PDA and  $\text{Fe}_3\text{O}_4$ @ $\text{SiO}_2$ -RITC- $\text{SiO}_2$  NPs seems similar, while fluorescent  $\text{Fe}_3\text{O}_4$ @ $\text{SiO}_2$ -FITC- $\text{SiO}_2$  NPs have lower internalization efficiency. This can be occasioned by the lower magnetization of FITC-MNPs compared to the other fluorescent single-core MNPs that experience a weaker attraction to the external magnets and are less efficient in cell transfection.

Moreover, the simultaneous transfection with different fluorescent MNPs was performed to assess the possibility to transfer different moieties for cell engineering in a single procedure. Figure 10 shows the transfection of HeLa cells with three different fluorescent MNPs in a single step as it can be corroborated by the emission signal produced by the different MNPs,  $\text{Fe}_3\text{O}_4$ @PDA (Figure 10a,  $\lambda = 424$  nm),  $\text{Fe}_3\text{O}_4$ @ $\text{SiO}_2$ -FITC- $\text{SiO}_2$  (Figure 10b,  $\lambda = 512$  nm) and  $\text{Fe}_3\text{O}_4$ @ $\text{SiO}_2$ -RITC (Figure 10c,  $\lambda = 583$  nm), and the merged emission of the three fluorescent entities, as observed in Figure 10d, within the same HeLa cells. This proof of concept shows that magnetic uptake allows a not only a fast transfection procedure (15 min of magnetic incubation versus several hours in passive transfection) but also the transfection of multiple moieties within a single and fast step that allows cost-effective bio-engineering processes which may prevent the degradation of proteins, drugs and cells when exposed to long incubation times [78–80].

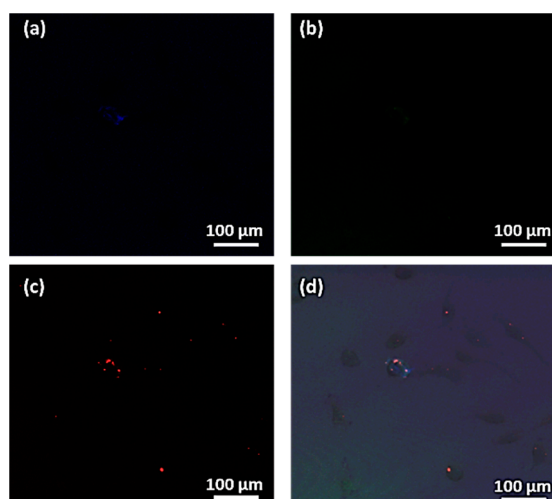


**Figure 10.** Representative image of confocal fluorescence micrographs of single core MNPs, (a)  $\text{Fe}_3\text{O}_4\text{@PDA}$ , (b)  $\text{Fe}_3\text{O}_4\text{@SiO}_2\text{-FITC-SiO}_2$  and (c)  $\text{Fe}_3\text{O}_4\text{@SiO}_2\text{-RITC-SiO}_2$ , and (d) the merged emission of the three MNPs internalized in living cells after the cell magnetic isolation.

### 3.6. Heat Capacity of Multi-Core MNPs for Magnetic Hyperthermia and Nanowarming

The use of external magnetic fields, besides being used to improve transfection and cell isolation processes, can also be used to generate heat on the nanoscale using MNPs through relaxation processes. To show the heating capability of MNPs, multi-core MNPs were employed and their response under exposure to external magnetic fields was studied to explore their capacity as nanoheaters in magnetic hyperthermia and nanowarming processes, using AC magnetometry measurements by commercial inductive magnetometers (AC Hyster Series; Nanotech Solutions, Madrid, Spain) with the application of a magnetic field of 20 kA/m at a frequency of 350, 300, 250 and 200 kHz. From the hysteresis loops obtained under these conditions, the values of  $H_C$ ,  $M_R$  and area, compiled in Table 3, were collected. To carry out the measurements, 40  $\mu\text{L}$  of the multi-core MNPs dispersed in water at a concentration of 5  $\text{g}_{\text{Fe}_3\text{O}_4}/\text{L}$  were used and their response was quantified by obtaining the specific absorption rate (SAR), denoted as  $\text{SAR}_{\text{AC}} = A \cdot f$ , where  $A$  is the magnetic area and  $f$  is AC magnetic field frequency.

**Table 3.** Coercivity ( $H_C$ ), remanence ( $M_R$ ) and maximum magnetization ( $M_{\text{max}}$ ) obtained by AC magnetometry; SAR values obtained by AC magnetometry ( $\text{SAR}_{\text{AC}}$ ) under the application of a magnetic field of 20  $\text{kAm}^{-1}$  at a frequency of 350 kHz and by magnetic hyperthermia processes ( $\text{SAR}_{\text{MH}}$ ); and temperature increases (from room temperature) obtained after 10 min under the application of a magnetic field of 20  $\text{kAm}^{-1}$  at a frequency of 605 kHz.

Sample	$H_{C\text{-AC}}$ ( $\text{kAm}^{-1}$ )	$M_{R\text{-AC}}$ ( $\text{Am}^2\text{kg}^{-1}$ )	$M_{\text{Max-AC}}$ ( $\text{Am}^2\text{kg}^{-1}$ )	Area ( $\text{mJkg}^{-1}$ )	$\text{SAR}_{\text{AC}}$ ( $\text{Wg}^{-1}$ )	$\text{SAR}_{\text{MH}}$ ( $\text{Wg}^{-1}$ )	$\Delta T$ ( $^{\circ}\text{C}$ )
$\text{Fe}_3\text{O}_4\text{@Cs}$	1.4	3.1	36.9	181.4	63.2	19.56	16.54
$\text{Fe}_3\text{O}_4\text{@Citrate}$	1.8	4.7	47.8	302.2	105.2	34.13	27.24
$\text{Fe}_3\text{O}_4\text{@SiO}_2$	3.8	4.5	22.4	288.5	100.5	34.55	24.37

Figure 11 shows the hysteresis loops obtained at an applied field of 20  $\text{kAm}^{-1}$  at four frequencies, 350, 300, 250 and 200 kHz, of the three multi-core MNPs:  $\text{Fe}_3\text{O}_4\text{@CS}$  (Figure 11a),  $\text{Fe}_3\text{O}_4\text{@Citrate}$  (Figure 11b) and  $\text{Fe}_3\text{O}_4\text{@SiO}_2$  (Figure 11c). From these hysteresis loops,  $H_C$ ,  $M_R$ ,  $M_{\text{Max}}$  and area values were obtained, which allows the  $\text{SAR}_{\text{AC}}$  to be obtained, revealing differences between multi-core MNPs. On the one hand, the maximum magnetization values differ from a minimum value of 22.4  $\text{Am}^2\text{kg}^{-1}$  (for  $\text{Fe}_3\text{O}_4\text{@SiO}_2$  MNPs) to a maximum of 47.8  $\text{Am}^2\text{kg}^{-1}$  (for  $\text{Fe}_3\text{O}_4\text{@Citrate}$  MNPs). Although the saturation values obtained by DC characterization at very high fields (10 kOe or 796  $\text{kAm}^{-1}$ )

revealed very similar  $M_S$  values in the multi-core MNPs, the maximum magnetization values and thus their response to lower field strengths ( $20 \text{ kAm}^{-1}$ ) differ from each other. This phenomenon may be because of precipitation and aggregation effects of the MNPs in liquid media during AC characterization processes, which, unlike DC measurements where the samples are in a powdered state, leads to a reduction in the magnetization of the MNPs [81,82]. The coercivity values revealed to be similar for the multi-core MNPs synthesized by the solvothermal method ( $1.4$  and  $1.8 \text{ kAm}^{-1}$  for  $\text{Fe}_3\text{O}_4@\text{CS}$  and  $\text{Fe}_3\text{O}_4@\text{Citrate}$ ) are higher for  $\text{Fe}_3\text{O}_4@\text{SiO}_2$  ( $3.8 \text{ kAm}^{-1}$ ). However, despite the high coercivity value of the  $\text{Fe}_3\text{O}_4@\text{SiO}_2$  MNPs, the lower magnetization ( $M_{\text{MAX}} = 22.4 \text{ Am}^2\text{kg}^{-1}$ ) means that the area obtained from these MNPs is not the highest of the three MNPs and, therefore, they do not have the highest SAR value ( $100.5 \text{ Wg}^{-1}$ ). Due to the higher magnetization of the  $\text{Fe}_3\text{O}_4@\text{Citrate}$  MNPs and, despite having a lower coercivity value than the  $\text{Fe}_3\text{O}_4@\text{SiO}_2$  MNPs, the area obtained is the largest of the three multi-core MNPs ( $A = 302.2 \text{ Am}^2\text{kg}^{-1}$ ), also obtaining the highest SAR value ( $105.2 \text{ Wg}^{-1}$ ). The  $\text{Fe}_3\text{O}_4@\text{CS}$ , however, reveals the lowest SAR value ( $63.2 \text{ Wg}^{-1}$ ), which corresponds to the lower values of  $1.4 \text{ kAm}^{-1}$  and  $3.1 \text{ kAm}^{-1}$ , giving an area of  $181.4 \text{ mJkg}^{-1}$ . It is also observed that the coercivity values are higher than those obtained by DC magnetometry ( $0.3$ ,  $1.4$  and  $0.8 \text{ kAm}^{-1}$ ), which is in agreement with the increase of coercivity with increasing frequency [83]. The dependence of  $\text{SAR}_{\text{AC}}$  on the four frequencies used is shown in Figure 11d, where a decay of SAR with frequency is generally observed.

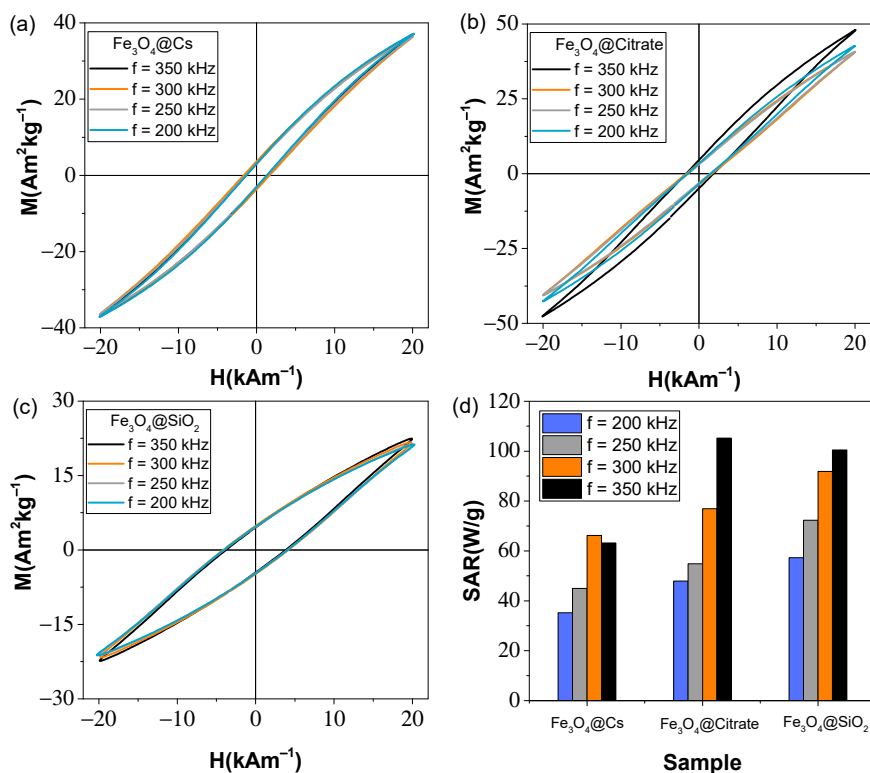


**Figure 11.** AC hysteresis curves under  $H_{\text{AC}}$  ( $20 \text{ kAm}^{-1}$ ) and four frequencies, 350 (black), 300 (orange), 250 (gray) and 200 (blue) kHz at room temperature for the multi-core MNPs: (a)  $\text{Fe}_3\text{O}_4@\text{CS}$ , (b)  $\text{Fe}_3\text{O}_4@\text{Citrate}$  and (c)  $\text{Fe}_3\text{O}_4@\text{SiO}_2$ . The iron oxide content was  $5 \text{ g}_{\text{Fe}_3\text{O}_4}/\text{L}$  for all measurements. (d) Specific absorption rate values were obtained by the AC hysteresis curves ( $\text{SAR}_{\text{NTSOL}}$ ) at the different frequencies.

The use of multi-core MNPs in magnetic hyperthermia processes has been explored using a commercially available setup (MagneTherm, Nanotherics) equipped with a fiber optic, operating at a fixed magnetic field of  $20 \text{ kAm}^{-1}$  and four different frequencies 605, 428, 252 and 168 kHz. Measurements were carried out by placing MNPs dispersed in

water (400  $\mu\text{L}$  at a concentration of 5 mg/mL) in the sample holder in the midpoint of a water-cooled hollow coil (maximum of RF magnetic field) and recording the temperature increase versus time with a fiber-optic thermometer during 10 min of magnetic field on and 2 min of magnetic field off. Figure 12 shows the heating curves of the multi-core MNPs,  $\text{Fe}_3\text{O}_4@\text{CS}$  (Figure 12a),  $\text{Fe}_3\text{O}_4@\text{Citrate}$  (Figure 12b) and  $\text{Fe}_3\text{O}_4@\text{SiO}_2$  (Figure 12c). The temperature increments at 10 min, recorded after the application of a  $20 \text{ kAm}^{-1}$  field at a frequency of 605 kHz (blue lines in Figure 12), compiled in Table 3, reveal increments of 16.54, 27.24 and  $24.37 \text{ }^\circ\text{C}$  (from room temperature,  $23 \text{ }^\circ\text{C}$ ), for the samples  $\text{Fe}_3\text{O}_4@\text{CS}$ ,  $\text{Fe}_3\text{O}_4@\text{Citrate}$  and  $\text{Fe}_3\text{O}_4@\text{SiO}_2$ , respectively, reaching temperatures valid for application of the multi-core MNPs in magnetic hyperthermia processes ( $42\text{--}45 \text{ }^\circ\text{C}$ ) [84].

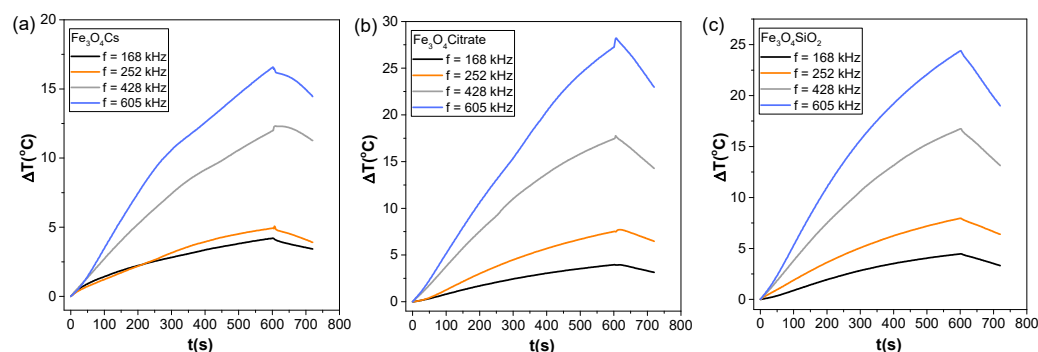


**Figure 12.** Heating curves of (a)  $\text{Fe}_3\text{O}_4@\text{CS}$ , (b)  $\text{Fe}_3\text{O}_4@\text{Citrate}$  and (c)  $\text{Fe}_3\text{O}_4@\text{SiO}_2$  under the application of a  $20 \text{ kAm}^{-1}$  magnetic field at different frequencies, 168 kHz (black), 252 kHz (grey), 428 kHz (orange) and 605 kHz (blue), for 10 min at a MNPs. The iron oxide content was  $5 \text{ g}_{\text{Fe}_3\text{O}_4}/\text{L}$  for all measurements.

From the heating curves observed in Figure 12 it was possible to study the heating efficiency by determining the SAR:

$$\text{SAR} = \chi_0 H_0^2 \mu_0 \pi \frac{2\pi f^2 \tau}{1 + (2\pi f \tau)^2} \quad (2)$$

where  $\chi_0$  is the initial susceptibility,  $H_0$  is the amplitude of the magnetic field,  $f$  is the frequency, and  $\tau$  is the effective relaxation time accounts for a combination of Néel ( $\tau_N$ ) and Brown ( $\tau_B$ ) relaxation times. The SAR was obtained experimentally using the following expression:

$$\text{SAR} = \frac{P}{m_{\text{NP}}} = \frac{Q}{\Delta t} = \frac{m_{\text{NP}} c_{\text{NP}} + m_{\text{water}} c_{\text{water}}}{m_{\text{NP}}} \left( \frac{\Delta T}{\Delta t} \right)_0 \quad (3)$$

where  $m_{\text{NP}}$  and  $m_{\text{water}}$  mass of iron oxide based MNPs and water were calculated from the total mass of each sample and, taking into account iron oxide weight percentage determined by FAAS or thermogravimetry analysis and  $c_{\text{NP}} = 0.746 \text{ (Jg}^{-1}\text{K}^{-1}\text{)}$  and  $c_{\text{water}} = 4.18 \text{ (Jg}^{-1}\text{K}^{-1}\text{)}$ , are, respectively, the specific heat of magnetite and water. The SAR values of the different MNPs, obtained from Equation (3) and compiled in Table 3, revealed values of 19.56, 34.13 and  $34.55 \text{ Wg}^{-1}$  for the  $\text{Fe}_3\text{O}_4@\text{CS}$ ,  $\text{Fe}_3\text{O}_4@\text{Citrate}$  and  $\text{Fe}_3\text{O}_4@\text{SiO}_2$  MNPs. These values present the same trend as those obtained by AC magnetometry ( $\text{SAR}_{\text{AC}}$ ) with the  $\text{Fe}_3\text{O}_4@\text{Citrate}$  and  $\text{Fe}_3\text{O}_4@\text{SiO}_2$  MNPs presenting the highest values and the  $\text{Fe}_3\text{O}_4@\text{CS}$  sample presenting a lower value, although they are significantly lower than those obtained by AC magnetometry. This is probably due to the larger volume used in the magnetic hyperthermia processes (400  $\mu\text{L}$ ), which makes heating more difficult.

#### 4. Conclusions

In this work, multifunctional single-core and multi-core MNPs, with average sizes from 8 to 200 nm, were synthesized using different bottom-up routes (co-precipitation,

solvothermal and thermal decomposition methods) functionalized by polymeric coatings, through in situ processes using synthesis methods, or by inorganic ( $\text{SiO}_2$ ) coatings, using the micro-emulsion method to design MNPs with a single core structure or the Stöber method to organize the magnetic cores into multi-core structures. Structural, morphological, colloidal stability and the magnetic characterizations of all MNPs were carried out using different experimental techniques, XRD, FTIR, TEM, DLS, FAAS, TGA, VSM and SQUID magnetometry, to assess the overall physicochemical properties achieved by synthetic control.

Thus, single-core MNPs, functionalized with fluorescent agents with emissions at different wavelengths (PDA, FITC and RITC) were developed with optical properties for cell labelling and multi-core MNPs, based on clustering of MNPs, were prepared as optimized systems for a nanoscale heat emission approach. Fluorescent single-core MNPs were tested as efficient carriers in magnetic transfection procedures revealing by confocal microscopy imaging, that, with a magnetic incubation of only 15 min and after the magnetic isolation of HeLa cells, different MNPs efficiently internalize in cells. Moreover, simultaneous transfection with different fluorescent MNPs (with PDA, RITC or FITC moieties) can be achieved, demonstrating the suitability of magnetic transfection for complex bioengineering procedures.

On the other hand, the efficiency of multi-core MNPs in heating processes was demonstrated by AC magnetometry study and by the application of external magnetic fields, exploring the heating efficiency for magnetic hyperthermia and nanowarming processes. In this case, it was observed that the heating efficiency varies notably, using the same synthesis method, the solvothermal one, but varying the reactive agents (citrate and CS) as well as the temperature and time, obtaining SAR values up to  $100 \text{ Wg}^{-1}$ . On the other hand, it was shown that the Stöber method can be used for the grouping of MNPs in clusters as a synthesis method with lower energy cost than the solvothermal method and with similar heating efficiencies.

**Supplementary Materials:** The following supporting information can be downloaded at: <https://www.mdpi.com/article/10.3390/magnetochemistry8080083/s1>; Figure S1. XRD patterns of  $\text{Fe}_3\text{O}_4$ @PEG NPs (wine pattern),  $\text{Fe}_3\text{O}_4$ @OA NPs, synthesized by decomposition method, DT (dark yellow pattern) and  $\text{Fe}_3\text{O}_4$ @OA NPs, synthesized by co-precipitation method, COP (grey pattern), compared to the XRD pattern of magnetite from the ICDS card No. 98-015-8742 data base; Figure S2. XRD patterns of  $\text{Fe}_3\text{O}_4$ @PEG NPs (wine pattern),  $\text{Fe}_3\text{O}_4$ @OA NPs, synthesized by decomposition method, DT (dark yellow pattern) and  $\text{Fe}_3\text{O}_4$ @OA NPs, synthesized by co-precipitation method, COP (grey pattern), compared to the XRD pattern of magnetite from the ICDS card No. 98-015-8742 data base; Figure S3. Representative TEM micrographs of  $\text{Fe}_3\text{O}_4$ @OA NPs, synthesized by co-precipitation method,  $\text{Fe}_3\text{O}_4$ @OA NPs, synthesized by decomposition method and  $\text{Fe}_3\text{O}_4$ @PEG NPs [58,62,85–87].

**Author Contributions:** Conceptualization—P.G.A., M.A.G.G. and Y.P.; supervision and formal analysis—Y.P.; writing—P.G.A., M.A.G.G., Á.A.P., L.D.C.A., R.S.G., Y.P. and J.R.; investigation and development—P.G.A., M.A.G.G., Á.A.P., L.D.C.A. and R.S.G.; supervision and group direction: J.R. All authors have read and agreed to the published version of the manuscript.

**Funding:** This work was supported by the European Commission under the BOW project (FETPROACT-EIC-05-2019, Grant 952183); partially supported by the Spanish Ministry of Science and Innovation (PID2020-112626RB-C21), Modalities “Research Challenges” and “Knowledge Generation”; and the Regional Consellería de Innovación Program for the Grupos de Referencia Competitiva 2021—GRC2021 project of Xunta de Galicia.

**Institutional Review Board Statement:** Not applicable.

**Informed Consent Statement:** Not applicable.

**Data Availability Statement:** Not applicable.

**Conflicts of Interest:** The authors declare no conflict of interest.

## References

1. Laurent, S.; Forge, D.; Port, M.; Roch, A.; Robic, C.; vander Elst, L.; Muller, R.N. Magnetic Iron Oxide Nanoparticles: Synthesis, Stabilization, Vectorization, Physicochemical Characterizations and Biological Applications. *Chem. Rev.* **2008**, *108*, 2064–2110. [[CrossRef](#)]
2. Arias, L.S.; Pessan, J.P.; Vieira, A.P.M.; de Lima, T.M.T.; Delbem, A.C.B.; Monteiro, D.R. Iron Oxide Nanoparticles for Biomedical Applications: A Perspective on Synthesis, Drugs, Antimicrobial Activity, and Toxicity. *Antibiotics* **2018**, *7*, 46. [[CrossRef](#)] [[PubMed](#)]
3. Yáñez-Vilar, S.; Sánchez-Andújar, M.; Gómez-Aguirre, C.; Mira, J.; Señaris-Rodríguez, M.A.; Castro-García, S. A Simple Solvothermal Synthesis of  $MFe_2O_4$  ( $M = Mn, Co$  and  $Ni$ ) Nanoparticles. *J. Solid State Chem.* **2009**, *182*, 2685–2690. [[CrossRef](#)]
4. Chen, Y.; Zhang, J.; Wang, Z.; Zhou, Z. Solvothermal Synthesis of Size-Controlled Monodispersed Superparamagnetic Iron Oxide Nanoparticles. *Appl. Sci.* **2019**, *9*, 5157. [[CrossRef](#)]
5. Ajinkya, N.; Yu, X.; Kaithal, P.; Luo, H.; Somani, P.; Ramakrishna, S. Magnetic Iron Oxide Nanoparticle (Ionp) Synthesis to Applications: Present and Future. *Materials* **2020**, *13*, 4644. [[CrossRef](#)]
6. de Montferrand, C.; Hu, L.; Milosevic, I.; Russier, V.; Bonnin, D.; Motte, L.; Brioude, A.; Lalatonne, Y. Iron Oxide Nanoparticles with Sizes, Shapes and Compositions Resulting in Different Magnetization Signatures as Potential Labels for Multiparametric Detection. *Acta Biomater.* **2013**, *9*, 6150–6157. [[CrossRef](#)]
7. Song, C.; Sun, W.; Xiao, Y.; Shi, X. Ultrasmall Iron Oxide Nanoparticles: Synthesis, Surface Modification, Assembly, and Biomedical Applications. *Drug Discov. Today* **2019**, *24*, 835–844. [[CrossRef](#)]
8. Li, S.; Zhang, T.; Tang, R.; Qiu, H.; Wang, C.; Zhou, Z. Solvothermal Synthesis and Characterization of Monodisperse Superparamagnetic Iron Oxide Nanoparticles. *J. Magn. Magn. Mater.* **2015**, *379*, 226–231. [[CrossRef](#)]
9. Gutiérrez, L.; Costo, R.; Grüttner, C.; Westphal, F.; Gehrke, N.; Heinke, D.; Fornara, A.; Pankhurst, Q.A.; Johansson, C.; Veintemillas-Verdaguer, S.; et al. Synthesis Methods to Prepare Single- and Multi-Core Iron Oxide Nanoparticles for Biomedical Applications. *Dalton Trans.* **2015**, *44*, 2943–2952. [[CrossRef](#)]
10. Liu, S.; Yu, B.; Wang, S.; Shen, Y.; Cong, H. Preparation, Surface Functionalization and Application of  $Fe_3O_4$  Magnetic Nanoparticles. *Adv. Colloid Interface Sci.* **2020**, *281*, 102165. [[CrossRef](#)]
11. Bean, C.P.; Livingston, J.D. Superparamagnetism. *J. Appl. Phys.* **1959**, *30*, S120–S129. [[CrossRef](#)]
12. Colombo, M.; Carregal-Romero, S.; Casula, M.F.; Gutiérrez, L.; Morales, M.P.; Böhm, I.B.; Heverhagen, J.T.; Prospero, D.; Parak, W.J. Biological Applications of Magnetic Nanoparticles. *Chem. Soc. Rev.* **2012**, *41*, 4306–4334. [[CrossRef](#)]
13. Israel, L.L.; Galstyan, A.; Holler, E.; Ljubimova, J.Y. Magnetic Iron Oxide Nanoparticles for Imaging, Targeting and Treatment of Primary and Metastatic Tumors of the Brain. *J. Control. Release* **2020**, *320*, 45–62. [[CrossRef](#)] [[PubMed](#)]
14. Zelepukin, I.V.; Yaremenko, A.V.; Ivanov, I.N.; Yuryev, M.V.; Cherkasov, V.R.; Deyev, S.M.; Nikitin, P.I.; Nikitin, M.P. Long-Term Fate of Magnetic Particles in Mice: A Comprehensive Study. *ACS Nano* **2021**, *15*, 11341–11357. [[CrossRef](#)] [[PubMed](#)]
15. Wu, K.; Su, D.; Saha, R.; Wong, D.; Wang, J.P. Magnetic Particle Spectroscopy-Based Bioassays: Methods, Applications, Advances, and Future Opportunities. *J. Phys. D Appl. Phys.* **2019**, *52*, 173001. [[CrossRef](#)]
16. Ramalho, J.; Ramalho, M.; Jay, M.; Burke, L.M.; Semelka, R.C. Gadolinium Toxicity and Treatment. *Magn. Reson. Imaging* **2016**, *34*, 1394–1398. [[CrossRef](#)] [[PubMed](#)]
17. Gradinaru, L.M.; Barbalata Mandru, M.; Drobotu, M.; Aflori, M.; Butnaru, M.; Spiridon, M.; Doroftei, F.; Aradoaei, M.; Ciobanu, R.C.; Vlad, S. Composite Materials Based on Iron Oxide Nanoparticles and Polyurethane for Improving the Quality of MRI. *Polymers* **2021**, *13*, 4316. [[CrossRef](#)]
18. Kader, A.; Kaufmann, J.O.; Mangarova, D.B.; Moeckel, J.; Brangsch, J.; Adams, L.C.; Zhao, J.; Reimann, C.; Saatz, J.; Traub, H.; et al. Iron Oxide Nanoparticles for Visualization of Prostate Cancer in MRI. *Cancers* **2022**, *14*, 2909. [[CrossRef](#)]
19. Wu, M.; Li, X.; Guo, Q.; Li, J.; Xu, G.; Li, G.; Wang, J.; Zhang, X. Magnetic Mesoporous Silica Nanoparticles-Aided Dual MR/NIRF Imaging to Identify Macrophage Enrichment in Atherosclerotic Plaques. *Nanomed. Nanotechnol. Biol. Med.* **2021**, *32*, 102330. [[CrossRef](#)]
20. Ledda, M.; Fioretti, D.; Lolli, M.G.; Papi, M.; di Gioia, C.; Carletti, R.; Ciasca, G.; Foglia, S.; Palmieri, V.; Marchese, R.; et al. Biocompatibility Assessment of Sub-5 Nm Silica-Coated Superparamagnetic Iron Oxide Nanoparticles in Human Stem Cells and in Mice for Potential Application in Nanomedicine. *Nanoscale* **2020**, *12*, 1759–1778. [[CrossRef](#)]
21. García, R.S.; Stafford, S.; Gun'ko, Y.K. Recent Progress in Synthesis and Functionalization of Multimodal Fluorescent-Magnetic Nanoparticles for Biological Applications. *Appl. Sci.* **2018**, *8*, 172. [[CrossRef](#)]
22. Molaei, M.J.; Salimi, E. Magneto-Fluorescent Superparamagnetic  $Fe_3O_4@SiO_2@alginate$ /Carbon Quantum Dots Nanohybrid for Drug Delivery. *Mater. Chem. Phys.* **2022**, *288*, 126361. [[CrossRef](#)]
23. Li, X.; Lin, H.; Li, Q.; Xue, J.; Xu, Y.; Zhuang, L. Recyclable Magnetic Fluorescent  $Fe_3O_4@SiO_2$ Core-Shell Nanoparticles Decorated with Carbon Dots for Fluoride Ion Removal. *ACS Appl. Nano Mater.* **2021**, *4*, 3062–3074. [[CrossRef](#)]
24. Siciliano, G.; Monteduro, A.G.; Turco, A.; Primiceri, E.; Rizzato, S.; Depalo, N.; Curri, M.L.; Maruccio, G. Polydopamine-Coated Magnetic Iron Oxide Nanoparticles: From Design to Applications. *Nanomaterials* **2022**, *12*, 1145. [[CrossRef](#)]
25. Lin, L.S.; Cong, Z.X.; Cao, J.B.; Ke, K.M.; Peng, Q.L.; Gao, J.; Yang, H.H.; Liu, G.; Chen, X. Multifunctional  $Fe_3O_4@polydopamine$  Core-Shell Nanocomposites for Intracellular mRNA Detection and Imaging-Guided Photothermal Therapy. *ACS Nano* **2014**, *8*, 3876–3883. [[CrossRef](#)] [[PubMed](#)]

26. Singh, N.; Sallem, F.; Mirjolet, C.; Nury, T.; Sahoo, S.K.; Millot, N.; Kumar, R. Polydopamine Modified Superparamagnetic Iron Oxide Nanoparticles as Multifunctional Nanocarrier for Targeted Prostate Cancer Treatment. *Nanomaterials* **2019**, *9*, 138. [[CrossRef](#)]
27. Singh, N.; Millot, N.; Maurizi, L.; Lizard, G.; Kumar, R. Taurine-Conjugated Mussel-Inspired Iron Oxide Nanoparticles with an Elongated Shape for Effective Delivery of Doxorubicin into the Tumor Cells. *ACS Omega* **2020**, *5*, 16165–16175. [[CrossRef](#)]
28. Shi, M.; Zhang, J.; Li, J.; Fan, Y.; Wang, J.; Sun, W.; Yang, H.; Peng, C.; Shen, M.; Shi, X. Polydopamine-Coated Magnetic Mesoporous Silica Nanoparticles for Multimodal Cancer Theranostics. *J. Mater. Chem. B* **2019**, *7*, 368–372. [[CrossRef](#)] [[PubMed](#)]
29. Morato, Y.L.; Paredes, K.O.; Chamizo, L.L.; Marciello, M.; Filice, M. Recent Advances in Multimodal Molecular Imaging of Cancer Mediated by Hybrid Magnetic Nanoparticles. *Polymers* **2021**, *13*, 2989. [[CrossRef](#)]
30. Chekina, N.; Horák, D.; Jendelová, P.; Trchová, M.; Bene, M.J.; Hrubý, M.; Herynek, V.; Turnovcová, K.; Syková, E. Fluorescent Magnetic Nanoparticles for Biomedical Applications. *J. Mater. Chem.* **2011**, *21*, 7630–7639. [[CrossRef](#)]
31. Lartigue, L.; Coupeau, M.; Lesault, M. Luminophore and Magnetic Multicore Nanoassemblies for Dual-Mode MRI and Fluorescence Imaging. *Nanomaterials* **2020**, *10*, 28. [[CrossRef](#)] [[PubMed](#)]
32. Piñeiro, Y.; Vargas, Z.; Rivas, J.; López-Quintela, M.A. Iron Oxide Based Nanoparticles for Magnetic Hyperthermia Strategies in Biological Applications. *Eur. J. Inorg. Chem.* **2015**, *2015*, 4495–4509. [[CrossRef](#)]
33. Chiu-Lam, A.; Staples, E.; Pepine, C.J.; Rinaldi, C. Perfusion, Cryopreservation, and Nanowarming of Whole Hearts Using Colloidally Stable Magnetic Cryopreservation Agent Solutions. *Sci. Adv.* **2021**, *7*, eabe3005.
34. Gao, Z.; Ring, H.L.; Sharma, A.; Namsrai, B.; Tran, N.; Finger, E.B.; Garwood, M.; Haynes, C.L.; Bischof, J.C. Preparation of Scalable Silica-Coated Iron Oxide Nanoparticles for Nanowarming. *Adv. Sci.* **2020**, *7*, 1901624. [[CrossRef](#)]
35. Ovejero, J.G.; Spizzo, F.; Morales, M.P.; del Bianco, L. Nanoparticles for Magnetic Heating: When Two (or More) Is Better than One. *Materials* **2021**, *14*, 6416. [[CrossRef](#)]
36. Qiu, P.; Jensen, C.; Charity, N.; Towner, R.; Mao, C. Oil Phase Evaporation-Induced Self-Assembly of Hydrophobic Nanoparticles into Spherical Clusters with Controlled Surface Chemistry in an Oil-in-Water Dispersion and Comparison of Behaviors of Individual and Clustered Iron Oxide Nanoparticles. *J. Am. Chem. Soc.* **2010**, *132*, 17724–17732. [[CrossRef](#)]
37. Chen, O.; Riedemann, L.; Etoc, F.; Herrmann, H.; Coppey, M.; Barch, M.; Farrar, C.T.; Zhao, J.; Bruns, O.T.; Wei, H.; et al. Magneto-Fluorescent Core-Shell Supernanoparticles. *Nat. Commun.* **2014**, *5*, 5093. [[CrossRef](#)] [[PubMed](#)]
38. Kong, S.D.; Choi, C.; Khamwannah, J.; Jin, S. Magnetically Vectored Delivery of Cancer Drug Using Remotely On-off Switchable Nano Capsules. *IEEE Trans. Magn.* **2013**, *49*, 349–352. [[CrossRef](#)]
39. Elsaïdy, A.; Vallejo, J.P.; Salgueiriño, V.; Lugo, L. Tuning the Thermal Properties of Aqueous Nanofluids by Taking Advantage of Size-Customized Clusters of Iron Oxide Nanoparticles. *J. Mol. Liq.* **2021**, *344*, 117727. [[CrossRef](#)]
40. Ranoo, S.; Lahiri, B.B.; Damodaran, S.P.; Philip, J. Tuning Magnetic Heating Efficiency of Colloidal Dispersions of Iron Oxide Nano-Clusters by Varying the Surfactant Concentration during Solvothermal Synthesis. *J. Mol. Liq.* **2022**, *360*, 119444. [[CrossRef](#)]
41. Foroozandeh, P.; Aziz, A.A. Insight into Cellular Uptake and Intracellular Trafficking of Nanoparticles. *Nanoscale Res. Lett.* **2018**, *13*, 339. [[CrossRef](#)] [[PubMed](#)]
42. Fu, R.; Yan, Y.; Roberts, C.; Liu, Z.; Chen, Y. The Role of Dipole Interactions in Hyperthermia Heating Colloidal Clusters of Densely-Packed Superparamagnetic Nanoparticles. *Sci. Rep.* **2018**, *8*, 4704. [[CrossRef](#)] [[PubMed](#)]
43. Skumiel, A.; Kertmen, A.; Nowaczyk, G. Investigation of the Magnetic Hyperthermia Effect in an Aqueous Dispersion of Colloidosomal Nanoparticle Clusters. *J. Mol. Liq.* **2019**, *283*, 91–95. [[CrossRef](#)]
44. Dutz, S.; Clement, J.H.; Eberbeck, D.; Gelbrich, T.; Hergt, R.; Müller, R.; Wotschadlo, J.; Zeisberger, M. Ferrofluids of Magnetic Multicore Nanoparticles for Biomedical Applications. *J. Magn. Magn. Mater.* **2009**, *321*, 1501–1504. [[CrossRef](#)]
45. Casula, M.F.; Conca, E.; Bakaimi, I.; Sathya, A.; Materia, M.E.; Casu, A.; Falqui, A.; Sogne, E.; Pellegrino, T.; Kanaras, A.G. Manganese doped-iron oxide nanoparticle clusters and their potential as agents for magnetic resonance imaging and hyperthermia. *Phys. Chem. Chem. Phys.* **2016**, *18*, 16848. [[CrossRef](#)]
46. Vamvakidis, K.; Mourdikoudis, S.; Makridis, A.; Paulidou, E.; Angelakeris, M.; Dendrinou-Samara, C. Magnetic Hyperthermia Efficiency and MRI Contrast Sensitivity of Colloidal Soft/Hard Ferrite Nanoclusters. *J. Colloid Interface Sci.* **2018**, *511*, 101–109. [[CrossRef](#)] [[PubMed](#)]
47. Liu, X.L.; Choo, E.S.G.; Ahmed, A.S.; Zhao, L.Y.; Yang, Y.; Ramanujan, R.V.; Xue, J.M.; di Fan, D.; Fan, H.M.; Ding, J. Magnetic Nanoparticle-Loaded Polymer Nanospheres as Magnetic Hyperthermia Agents. *J. Mater. Chem. B* **2014**, *2*, 120–128. [[CrossRef](#)] [[PubMed](#)]
48. Shabatina, T.I.; Vernaya, O.I.; Shabatin, V.P.; Melnikov, M.Y. Magnetic Nanoparticles for Biomedical Purposes: Modern Trends and Prospects. *Magnetochemistry* **2020**, *6*, 30. [[CrossRef](#)]
49. Piñeiro, Y.; Gómez, M.G.; Alves, L.d.C.; Prieto, A.A.; Acevedo, P.G.; Gudiña, R.S.; Puig, J.; Teijeiro, C.; Vilar, S.Y.; Rivas, J. Hybrid Nanostructured Magnetite Nanoparticles: From Bio-Detection and Theragnostics to Regenerative Medicine. *Magnetochemistry* **2020**, *6*, 4. [[CrossRef](#)]
50. Massart, R. Preparation of Aqueous Magnetic Liquids in Alkaline and Acidic Media. *IEEE Trans. Magn.* **1981**, *17*, 1247–1248. [[CrossRef](#)]
51. Zhou, Z.; Zhu, X.; Wu, D.; Chen, Q.; Huang, D.; Sun, C.; Xin, J.; Ni, K.; Gao, J. Anisotropic Shaped Iron Oxide Nanostructures: Controlled Synthesis and Proton Relaxation Shortening Effects. *Chem. Mater.* **2015**, *27*, 3505–3515. [[CrossRef](#)]

52. Fang, Y.; Loc, W.S.; Lu, W.; Fang, J. Synthesis of In<sub>2</sub>O<sub>3</sub>@SiO<sub>2</sub> Core-Shell Nanoparticles with Enhanced Deeper Energy Level Emissions of In<sub>2</sub>O<sub>3</sub>. *Langmuir* **2011**, *27*, 14091–14095. [[CrossRef](#)]
53. Han, Y.; Jiang, J.; Lee, S.S.; Ying, J.Y. Reverse Microemulsion-Mediated Synthesis of Silica-Coated Gold and Silver Nanoparticles. *Langmuir* **2008**, *24*, 5842–5848. [[CrossRef](#)] [[PubMed](#)]
54. Shen, M.; Jia, W.; Lin, C.; Fan, G.; Jin, Y.; Chen, X.; Chen, G. Facile Synthesis of Folate-Conjugated Magnetic/Fluorescent Bifunctional Microspheres. *Nanoscale Res. Lett.* **2014**, *9*, 558. [[CrossRef](#)] [[PubMed](#)]
55. Jiang, X.; Wang, F.; Cai, W.; Zhang, X. Trisodium Citrate-Assisted Synthesis of Highly Water-Dispersible and Superparamagnetic Mesoporous Fe<sub>3</sub>O<sub>4</sub> Hollow Microspheres via Solvothermal Process. *J. Alloys Compd.* **2015**, *636*, 34–39. [[CrossRef](#)]
56. Alavi Nikje, M.M.; Farahmand Nejad, M.A.; Shabani, K.; Haghshenas, M. Preparation of Magnetic Polyurethane Rigid Foam Nanocomposites. *Colloid Polym. Sci.* **2013**, *291*, 903–909. [[CrossRef](#)]
57. Saleh, T.A. Structural Characterization of Hybrid Materials. In *Polymer Hybrid Materials and Nanocomposites*; Elsevier: Amsterdam, The Netherlands, 2021; pp. 213–240.
58. Coker, V.S.; Bell, A.M.T.; Pearce, C.I.; Patrick, R.A.D.; van der Laan, G.; Lloyd, J.R. Time-Resolved Synchrotron Powder X-Ray Diffraction Study of Magnetite Formation by the Fe(III)-Reducing Bacterium *Geobacter Sulfurreducens*. *Am. Mineral.* **2008**, *93*, 540–547. [[CrossRef](#)]
59. Chitra, K.; Annadurai, G. Fluorescent Silica Nanoparticles in the Detection and Control of the Growth of Pathogen. *J. Nanotechnol.* **2013**, *2013*, 509628. [[CrossRef](#)]
60. Kumar, S.; Dutta, P.K.; Koh, J. A Physico-Chemical and Biological Study of Novel Chitosan-Chloroquinoline Derivative for Biomedical Applications. *Int. J. Biol. Macromol.* **2011**, *49*, 356–361. [[CrossRef](#)] [[PubMed](#)]
61. Li, Y.S.; Church, J.S.; Woodhead, A.L. Infrared and Raman Spectroscopic Studies on Iron Oxide Magnetic Nano-Particles and Their Surface Modifications. *J. Magn. Magn. Mater.* **2012**, *324*, 1543–1550. [[CrossRef](#)]
62. Rajan, A.; Sharma, M.; Sahu, N.K. Assessing Magnetic and Inductive Thermal Properties of Various Surfactants Functionalised Fe<sub>3</sub>O<sub>4</sub> Nanoparticles for Hyperthermia. *Sci. Rep.* **2020**, *10*, 15045. [[CrossRef](#)] [[PubMed](#)]
63. Cheng, W.; Fan, F.; Zhang, Y.; Pei, Z.; Wang, W.; Pei, Y. A Facile Approach for Fabrication of Core-Shell Magnetic Molecularly Imprinted Nanospheres towards Hypericin. *Polymers* **2017**, *9*, 135. [[CrossRef](#)] [[PubMed](#)]
64. Haddad, P.S.; Duarte, E.L.; Baptista, M.S.; Goya, G.F.; Leite, C.A.P.; Itri, R. Synthesis and Characterization of Silica-Coated Magnetic Nanoparticles. In *Surface and Colloid Science; Progress in Colloid and Polymer Science*; Springer: Berlin/Heidelberg, Germany, 2004; Volume 128, pp. 232–238.
65. Bhattacharjee, S. DLS and Zeta Potential—What They Are and What They Are Not? *J. Control. Release* **2016**, *235*, 337–351. [[CrossRef](#)] [[PubMed](#)]
66. Mazario, E.; Sánchez-Marcos, J.; Menéndez, N.; Herrasti, P.; García-Hernández, M.; Muñoz-Bonilla, A. One-Pot Electrochemical Synthesis of Polydopamine Coated Magnetite Nanoparticles. *RSC Adv.* **2014**, *4*, 48353–48361. [[CrossRef](#)]
67. Wu, Y.; Yang, W.; Wang, C.; Hu, J.; Fu, S. Chitosan Nanoparticles as a Novel Delivery System for Ammonium Glycyrrhizinate. *Int. J. Pharm.* **2005**, *295*, 235–245. [[CrossRef](#)]
68. Sikora, A.; Shard, A.G.; Minelli, C. Size and ζ-Potential Measurement of Silica Nanoparticles in Serum Using Tunable Resistive Pulse Sensing. *Langmuir* **2016**, *32*, 2216–2224. [[CrossRef](#)] [[PubMed](#)]
69. Franco-Ulloa, S.; Tatulli, G.; Bore, S.L.; Moglianetti, M.; Pompa, P.P.; Cascella, M.; de Vivo, M. Dispersion State Phase Diagram of Citrate-Coated Metallic Nanoparticles in Saline Solutions. *Nat. Commun.* **2020**, *11*, 5422. [[CrossRef](#)] [[PubMed](#)]
70. Lin, Z.; Luo, S.; Xu, D.; Liu, S.; Wu, N.; Yao, W.; Zhang, X.; Zheng, L.; Lin, X. Silica-Polydopamine Hybrids as Light-Induced Oxidase Mimics for Colorimetric Detection of Pyrophosphate. *Analyst* **2020**, *145*, 424–433. [[CrossRef](#)]
71. Wu, S.; Li, Z.; Han, J.; Han, S. Dual Colored Mesoporous Silica Nanoparticles with PH Activable Rhodamine-Lactam for Ratiometric Sensing of Lysosomal Acidity. *Chem. Commun.* **2011**, *47*, 11276–11278. [[CrossRef](#)]
72. Vargas-Osorio, Z.; da Silva-Candal, A.; Piñero, Y.; Iglesias-Rey, R.; Sobrino, T.; Campos, F.; Castillo, J.; Rivas, J. Multifunctional Superparamagnetic Stiff Nanoreservoirs for Blood Brain Barrier Applications. *Nanomaterials* **2019**, *9*, 449. [[CrossRef](#)] [[PubMed](#)]
73. Kucheryavy, P.; He, J.; John, V.T.; Maharjan, P.; Spinu, L.; Goloverda, G.Z.; Kolesnichenko, V.L. Superparamagnetic Iron Oxide Nanoparticles with Variable Size and an Iron Oxidation State as Prospective Imaging Agents. *Langmuir* **2013**, *29*, 710–716. [[CrossRef](#)] [[PubMed](#)]
74. Ramos-Docampo, M.A.; Testa-Anta, M.; Rivas-Murias, B.; Salgueiriño, V. Clusters of Magnetite-Maghemite Nanocrystals with a Chemically-Tailored Average Diameter. *J. Nanosci. Nanotechnol.* **2019**, *19*, 4930–4937. [[CrossRef](#)] [[PubMed](#)]
75. Smolensky, E.D.; Park, H.Y.E.; Zhou, Y.; Rolla, G.A.; Marjańska, M.; Botta, M.; Pierre, V.C. Scaling Laws at the Nanosize: The Effect of Particle Size and Shape on the Magnetism and Relaxivity of Iron Oxide Nanoparticle Contrast Agents. *J. Mater. Chem. B* **2013**, *1*, 2818–2828. [[CrossRef](#)] [[PubMed](#)]
76. Rivas Rojas, P.C.; Tancredi, P.; Moscoso Londoño, O.; Knobel, M.; Socolovsky, L.M. Tuning Dipolar Magnetic Interactions by Controlling Individual Silica Coating of Iron Oxide Nanoparticles. *J. Magn. Magn. Mater.* **2018**, *451*, 688–696. [[CrossRef](#)]
77. Bi, Q.; Song, X.; Hu, A.; Luo, T.; Jin, R.; Ai, H.; Nie, Y. Magnetofection: Magic Magnetic Nanoparticles for Efficient Gene Delivery. *Chin. Chem. Lett.* **2020**, *31*, 3041–3046. [[CrossRef](#)]
78. Ni, J.S.; Li, Y.; Yue, W.; Liu, B.; Li, K. Nanoparticle-Based Cell Trackers for Biomedical Applications. *Theranostics* **2020**, *10*, 1923–1947. [[CrossRef](#)] [[PubMed](#)]

79. Sajib, M.; Albers, E.; Langeland, M.; Undeland, I. Understanding the Effect of Temperature and Time on Protein Degree of Hydrolysis and Lipid Oxidation during Ensilaging of Herring (*Clupea harengus*) Filleting Co-Products. *Sci. Rep.* **2020**, *10*, 9590. [[CrossRef](#)]
80. Graf, C.; Gao, Q.; Schütz, I.; Noufele, C.N.; Ruan, W.; Posselt, U.; Korotianskiy, E.; Nordmeyer, D.; Rancan, F.; Hadam, S.; et al. Surface Functionalization of Silica Nanoparticles Supports Colloidal Stability in Physiological Media and Facilitates Internalization in Cells. *Langmuir* **2012**, *28*, 7598–7613. [[CrossRef](#)]
81. Cabrera, D.; Coene, A.; Leliaert, J.; Artés-Ibáñez, E.J.; Dupré, L.; Telling, N.D.; Teran, F.J. Dynamical Magnetic Response of Iron Oxide Nanoparticles Inside Live Cells. *ACS Nano* **2018**, *12*, 2741–2752. [[CrossRef](#)] [[PubMed](#)]
82. Ovejero, J.G.; Cabrera, D.; Carrey, J.; Valdivielso, T.; Salas, G.; Teran, F.J. Effects of Inter- and Intra-Aggregate Magnetic Dipolar Interactions on the Magnetic Heating Efficiency of Iron Oxide Nanoparticles. *Phys. Chem. Chem. Phys.* **2016**, *18*, 10954–10963. [[CrossRef](#)] [[PubMed](#)]
83. Shah, S.A.; Reeves, D.B.; Ferguson, R.M.; Weaver, J.B.; Krishnan, K.M. Mixed Brownian Alignment and Néel Rotations in Superparamagnetic Iron Oxide Nanoparticle Suspensions Driven by an Ac Field. *Phys. Rev. B Condens. Matter Mater. Phys.* **2015**, *92*, 094438. [[CrossRef](#)] [[PubMed](#)]
84. Dutz, S.; Hergt, R. Magnetic Nanoparticle Heating and Heat Transfer on a Microscale: Basic Principles, Realities and Physical Limitations of Hyperthermia for Tumour Therapy. *Int. J. Hyperth.* **2013**, *29*, 790–800. [[CrossRef](#)] [[PubMed](#)]
85. Wei, Y.; Han, B.; Hu, X.; Lin, Y.; Wang, X.; Deng, X. Synthesis of Fe<sub>3</sub>O<sub>4</sub> Nanoparticles and Their Magnetic Properties. *Procedia Eng.* **2012**, *27*, 632–637. [[CrossRef](#)]
86. Yang, K.; Peng, H.; Wen, Y.; Li, N. Re-Examination of Characteristic FTIR Spectrum of Secondary Layer in Bilayer Oleic Acid-Coated Fe<sub>3</sub>O<sub>4</sub> Nanoparticles. *Appl. Surf. Sci.* **2010**, *256*, 3093–3097. [[CrossRef](#)]
87. Gopal, S.V.; Chitrambalam, S.; Joe, I.H. Coherent Source Interaction, Third-Order Nonlinear Response of Synthesized PEG Coated Magnetite Nanoparticles in Polyethylene Glycol and Its Application. *Opt. Laser Technol.* **2018**, *98*, 84–91. [[CrossRef](#)]